Spectral Fingerprints of Earth-like Planets Around FGK Stars

Sarah Rugheimer,[1] Lisa Kaltenegger,[1,2] Andras Zsom,[2,3] Antígona Segura,[4] and Dimitar Sasselov[1]

Abstract

We present model atmospheres for an Earth-like planet orbiting the entire grid of main sequence FGK stars with effective temperatures ranging from $T_{eff} = 4250$ K to $T_{eff} = 7000$ K in 250 K intervals. We have modeled the remotely detectable spectra of Earth-like planets for clear and cloudy atmospheres at the 1 AU equivalent distance from the VIS to IR (0.4 to 20 μm) to compare detectability of features in different wavelength ranges in accordance with the James Webb Space Telescope and future design concepts to characterize exo-Earths. We have also explored the effect of the stellar UV levels as well as spectral energy distribution on a terrestrial atmosphere, concentrating on detectable atmospheric features that indicate habitability on Earth, namely, H_2O, O_3, CH_4, N_2O, and CH_3Cl.

The increase in UV dominates changes of O_3, OH, CH_4, N_2O, and CH_3Cl, whereas the increase in stellar temperature dominates changes in H_2O. The overall effect as stellar effective temperatures and corresponding UV increase is a lower surface temperature of the planet due to a bigger part of the stellar flux being reflected at short wavelengths, as well as increased photolysis. Earth-like atmosphere models show more O_3 and OH but less stratospheric CH_4, N_2O, CH_3Cl, and tropospheric H_2O (but more stratospheric H_2O) with increasing effective temperature of main sequence stars. The corresponding detectable spectral features, on the other hand, show different detectability depending on the wavelength observed.

We concentrate on directly imaged planets here as a framework to interpret future light curves, direct imaging, and secondary eclipse measurements of atmospheres of terrestrial planets in the habitable zone at varying orbital positions. Key Words: Habitability—Planetary atmospheres—Extrasolar terrestrial planets—Spectroscopic biosignatures. Astrobiology 13, 251–269.

1. Introduction

OVER 830 EXTRASOLAR PLANETS have been found to date with thousands more candidate planets awaiting confirmation from NASA's Kepler mission. Several of these planets have been found in or near the circumstellar habitable zone (see, *e.g.,* Udry *et al.,* 2007; Borucki *et al.,* 2011; Kaltenegger and Sasselov, 2011; Batalha *et al.,* 2012) with masses and radii consistent with rocky planet models. Recent radial velocity results as well as Kepler observations demonstrate that small planets in the habitable zone exist around solar-type stars. Future mission concepts to characterize Earth-like planets are designed to take spectra of extrasolar planets with the ultimate goal of remotely detecting atmospheric signatures (*e.g.,* Beichman *et al.,* 1999, 2006; Cash, 2006; Traub *et al.,*

2006). For transiting terrestrial planets around the closest stars, the James Webb Space Telescope (JWST, see Gardner *et al.,* 2006), as well as future ground- and space-based telescopes, might be able to detect biosignatures by adding multiple transits for the closest stars (see Discussion).

Several groups have explored the effect of stellar spectral types on the atmospheric composition of Earth-like planets by considering specific stars: F9V and K2V (Selsis, 2000), F2V and K2V (Segura *et al.,* 2003; Grenfell *et al.,* 2007; Kitzmann *et al.,* 2011a, 2011b). In the present study, we expanded on this work by establishing planetary atmosphere models for the full FGK main sequence, using a stellar temperature grid from 7000 to 4250 K, in increments of 250 K, to explore the effect of the stellar types on terrestrial atmosphere models. We show the effects of stellar UV and stellar temperature on

[1]Harvard Smithsonian Center for Astrophysics, Cambridge, Massachusetts, USA.
[2]MPIA, Heidelberg, Germany.
[3]Department of Earth, Atmospheric and Planetary Sciences, Massachusetts Institute of Technology, Cambridge, Massachusetts, USA.
[4]Instituto de Ciencias Nucleares, Universidad Nacional Autónoma de México, México, D.F., México.

the planet's atmosphere individually to understand the overall effect of the stellar type on the remotely detectable planetary spectrum from 0.4 to 20 μm for clear and cloudy atmosphere models. This stellar temperature grid covers the full FGK spectral range and corresponds roughly to F0V, F2V, F5V, F7V, F9V/G0V, G2V, G8V, K0V, K2V, K4V, K5V, and K7V main sequence stars (following the spectral type classification by Gray, 1992).

In this paper, we use "Earth-like," as applied to our models, to mean using modern Earth's outgassing rates (following Segura *et al.,* 2003). We explore the influence of stellar spectral energy distribution (SED) on the chemical abundance and planetary atmospheric spectral features for Earth-like planets, including biosignatures and their observability from the VIS to IR. Atmospheric biosignatures are chemical species in the atmosphere that are out of chemical equilibrium or are by-products of life processes. In our analysis, we focused particularly on spectral features of chemical species that indicate habitability for a temperate rocky planet like Earth, H_2O, O_3, CH_4, N_2O, and CH_3Cl (Lovelock, 1975; Sagan *et al.,* 1993).

In Section 1, we introduce the photochemistry of an Earth-like atmosphere. In Section 2, we describe our model for calculating the stellar spectra, atmospheric models, and planetary spectra. Section 3 presents the influence of stellar types on the abundance of various atmospheric chemical species. In Section 4, we examine the remote observability of such spectral features, and in Sections 5 and 6, we conclude by summarizing the results and discussing their implications.

1.1. Photochemistry for Earth-like planets including potential biosignatures

For an Earth-like biosphere, the main detectable atmospheric chemical signatures that, in combination, could indicate habitability are O_2/O_3 with CH_4/N_2O, and CH_3Cl. Note that one spectral feature, for example, O_2, does not constitute a biosignature by itself, as the planetary context (like bulk planet, atmospheric composition, and planet insolation) must be taken into account to interpret this signature. Detecting high concentrations of a reducing gas concurrently with O_2 or O_3 can be used as a biosignature since reduced gases and oxygen react rapidly with each other. Both being present in significant and therefore detectable amounts in low-resolution spectra implies a strong source of both. In the IR, O_3 can be used as a proxy for oxygen at 10^{-2} present atmospheric level of O_2; the depth of the 9.6 μm O_3 feature is comparable to the modern atmospheric level (Kasting *et al.,* 1985; Segura *et al.,* 2003). At the same time, because of the 9.6 μm O_3 feature's nonlinear dependence on the O_2 concentration, observing in the VIS at 0.76 μm would be a more accurate O_2 level indicator but requires higher resolution than detecting O_3.

N_2O and CH_3Cl are both primarily produced by life on Earth with no strong abiotic sources; however, their spectral features are likely too small to detect in low resolution with the first generation of missions. While H_2O or CO_2 are not considered biosignatures, as both are produced through abiotic processes, they are important indicators of habitability as raw materials and can indicate the level of greenhouse effect on a planet. We refer the reader to other work (*e.g.,* Des Marais *et al.,* 2002; Meadows, 2006; Kaltenegger

et al., 2010a) for a more in-depth discussion on habitability and biosignatures. In this section, we briefly discuss the most important photochemical reactions involving H_2O, O_2, O_3, CH_4, N_2O, and CH_3Cl.
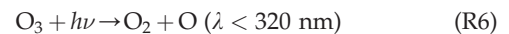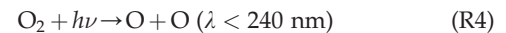
Water, H_2O: Water vapor is an important greenhouse gas in Earth's atmosphere. Over 99% of H_2O vapor is currently in the troposphere, where it is an important source of OH via the following set of reactions:

$$O_3 + h\nu \rightarrow O_2 + O(^1D) \tag{R1}$$

$$H_2O + O(^1D) \rightarrow 2OH \tag{R2}$$

In the troposphere, the production of $O(^1D)$ takes place for $3000\,\text{Å} < \lambda < 3200\,\text{Å}$, the lower limit of which is set by the inability of wavelengths, λ, shorter than 3000 Å to reach the troposphere due to O_3 shielding. H_2O, while photochemically inert in the troposphere, can be removed by photolysis primarily by wavelengths shortward of 2000 Å in the stratosphere. The photodissociation threshold energy is 2398 Å, but the cross section of the molecule above 2000 Å is very low. Stratospheric H_2O can be transported from the troposphere or formed in the stratosphere by CH_4 and OH.

$$CH_4 + OH \rightarrow CH_3 + H_2O \tag{R3}$$
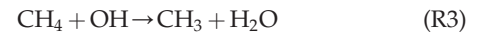
Oxygen and ozone, O_2 and O_3: In an atmosphere containing O_2, O_3 concentrations are determined by the absorption of UV light shortward of 2400 Å in the stratosphere. O_3 is an oxidizing agent more reactive than O_2, the most stable form of oxygen, due to the third oxygen atom being loosely bound by a single bond. O_3 is also an indirect measure of OH since reactions involving O_3 and H_2O are sources of OH. OH is very reactive and is the main sink for reducing species such as CH_4. O_3 is formed primarily by the Chapman reactions (1930) of the photolysis of O_2 by UV photons (1850 Å $< \lambda <$ 2420 Å) and then the combining of O_2 with O.

$$O_2 + h\nu \rightarrow O + O \ (\lambda < 240 \text{ nm}) \tag{R4}$$

$$O + O_2 + M \rightarrow O_3 + M \tag{R5}$$

$$O_3 + h\nu \rightarrow O_2 + O \ (\lambda < 320 \text{ nm}) \tag{R6}$$

$$O_3 + O \rightarrow 2O_2 \tag{R7}$$

where M is any background molecule such as O_2 or N_2. Reactions R5 and R6 are relatively fast compared with R4 and R7, which are the limiting reactions in Earth's atmosphere. However, considering the Chapman mechanism alone would overpredict the concentration of O_3 by a factor of 2 on Earth. Hydrogen oxide (HO_x), nitrogen oxide (NO_x), and chlorine (ClO_x) radicals are the additional sinks controlling the O_3 abundance (Bates and Nicolet, 1950; Crutzen, 1970; Molina and Rowland, 1974, respectively), with NO_x and HO_x being the dominant and second-most-dominant sinks, respectively.
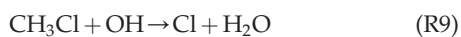
Methane, CH_4: Since CH_4 is a reducing gas, it reacts with oxidizing species and thus has a short lifetime of around 10–12 years in modern Earth's atmosphere (Houghton *et al.*, 1994). In both the troposphere and stratosphere, CH_4 is oxidized by OH, which is the largest sink of the global methane budget. In the stratosphere, CH_4 is also destroyed by UV radiation. Though its photodissociation energy is 2722 Å, its absorption cross section is not sufficient for $\lambda > 1500$ Å. CH_4 is produced biotically by methanogens and termites and abiotically through hydrothermal vent systems. In the modern atmosphere, there is a significant anthropogenic source of CH_4 from natural gas, livestock, and rice paddies. CH_4 is $25 \times$ more effective as a greenhouse gas than CO_2 in modern Earth's atmosphere (Forster *et al.*, 2007) and may have been much more abundant in early Earth (see, *e.g.*, Pavlov *et al.*, 2003).

Nitrous oxide, N_2O: N_2O is a relatively minor constituent of the modern atmosphere at around 320 ppbv, with a pre-industrial concentration of 270 ppbv (Forster *et al.*, 2007). It is important for stratospheric chemistry since around 5% is converted to NO, an important sink of O_3, and 95% produces N_2.

$$N_2O + O(^1D) \rightarrow 2NO \qquad (R8)$$

On current Earth, N_2O is emitted primarily by denitrifying bacteria with anthropogenic sources from fertilizers in agriculture, biomass burning, industry, and livestock.

Methyl chloride, CH_3Cl: CH_3Cl has been proposed as a potential biosignature because its primary sources are marine organisms, reactions of sea foam and light, and biomass burning (Segura *et al.*, 2005). The primary loss of CH_3Cl in Earth's atmosphere is by OH as seen in R9, but it can also be photolyzed or react with atomic chlorine. Because CH_3Cl is a source of chlorine in the stratosphere, it also plays a role in the removal of O_3 as discussed earlier.

$$CH_3Cl + OH \rightarrow Cl + H_2O \qquad (R9)$$

$$CH_3Cl + h\nu \rightarrow CH_3 + Cl \qquad (R10)$$

$$CH_3Cl + Cl \rightarrow HCl + Cl \qquad (R11)$$

2. Model Description

We use EXO-P (Kaltenegger and Sasselov 2010), a coupled one-dimensional radiative transfer atmosphere code developed for rocky exoplanets based on a 1-D climate (Kasting and Ackerman, 1986; Pavlov *et al.*, 2000; Haqq-Misra *et al.*, 2008), 1-D photochemistry (Pavlov and Kasting, 2002; Segura *et al.*, 2005, 2007), and 1-D radiative transfer model (Traub and Stier, 1976; Kaltenegger and Traub, 2009) to calculate the model spectrum of an Earth-like exoplanet.

2.1. Planetary atmosphere model

EXO-P is a model that simulates both the effects of stellar radiation on a planetary environment and the planet's outgoing spectrum. The altitude range extends to 60 km with

100 layers. We use a geometrical model in which the average 1-D global atmosphere model profile is generated by using a plane parallel atmosphere, treating the planet as a Lambertian sphere, and setting the stellar zenith angle to 60° to represent the average incoming stellar flux on the dayside of the planet (see also Schindler and Kasting, 2000). The temperature in each layer is calculated from the difference between the incoming and outgoing flux and the heat capacity of the atmosphere in each layer. If the lapse rate of a given layer is larger than the adiabatic lapse rate, it is adjusted to the adiabat until the atmosphere reaches equilibrium. A two-stream approximation (see Toon *et al.*, 1989), which includes multiple scattering by atmospheric gases, is used in the VIS/near IR to calculate the shortwave fluxes. Four-term, correlated-*k* coefficients parameterize the absorption by O_3, H_2O, O_2, and CH_4 in wavelength intervals shown in Fig. 1 (Pavlov *et al.*, 2000). In the thermal IR region, a rapid radiative transfer model calculates the longwave fluxes. Clouds are not explicitly calculated. The effects of clouds on the temperature/pressure profile are included by adjusting the surface albedo of the Earth-Sun system to have a surface temperature of 288 K (see Kasting *et al.*, 1984; Pavlov *et al.*, 2000; Segura *et al.*, 2003, 2005). The photochemistry code, originally developed by Kasting *et al.* (1985), solves for 55 chemical species linked by 220 reactions with a reverse-Euler method (see Segura *et al.*, 2010, and references therein).

The radiative transfer model used to compute planetary spectra is based on a model originally developed for trace gas retrieval in Earth's atmospheric spectra (Traub and Stier, 1976) and further developed for exoplanet transmission and emergent spectra (Kaltenegger *et al.*, 2007; Kaltenegger and Traub, 2009; Kaltenegger, 2010; Kaltenegger and Sasselov, 2010, 2011). In this paper, we model Earth's reflected and thermal emission spectra, using 21 of the most spectroscopically significant molecules (H_2O, O_3, O_2, CH_4, CO_2, OH, CH_3Cl, NO_2, N_2O, HNO_3, CO, H_2S, SO_2, H_2O_2, NO, ClO, HOCl, HO_2, H_2CO, N_2O_5, and HCl).

With 34 layers, the spectrum is calculated at high spectral resolution, with several points per line width, where the line shapes and widths are computed by Doppler and pressure broadening on a line-by-line basis, for each layer in the model atmosphere. The overall high-resolution spectrum is calculated with 0.1 cm^{-1} wave-number steps. The figures are shown smoothed to a resolving power of 250 in the IR and 800 in the VIS with a triangular smoothing kernel. The spectra may further be binned corresponding to proposed future spectroscopy mission designs to characterize Earth-like planets.

2.2. Model validation with EPOXI

We previously validated EXO-P from the VIS to the IR with data from ground and space (Kaltenegger *et al.*, 2007). Here, we use new data by EPOXI in the VIS and near IR (Livengood *et al.*, 2011) for further validation (see Fig. 2). The data set we use to validate our VIS and the near-IR Earth model spectra is the first EPOXI observation of Earth, which was averaged over 24 h on 03/18/2008–03/19/2008 and taken at a phase angle of 57.7°. Atmospheric models found the best match to be for a 50% cloud coverage with 1.5 km and 8.5 km cloud layer, respectively (Robinson *et al.*, 2011).
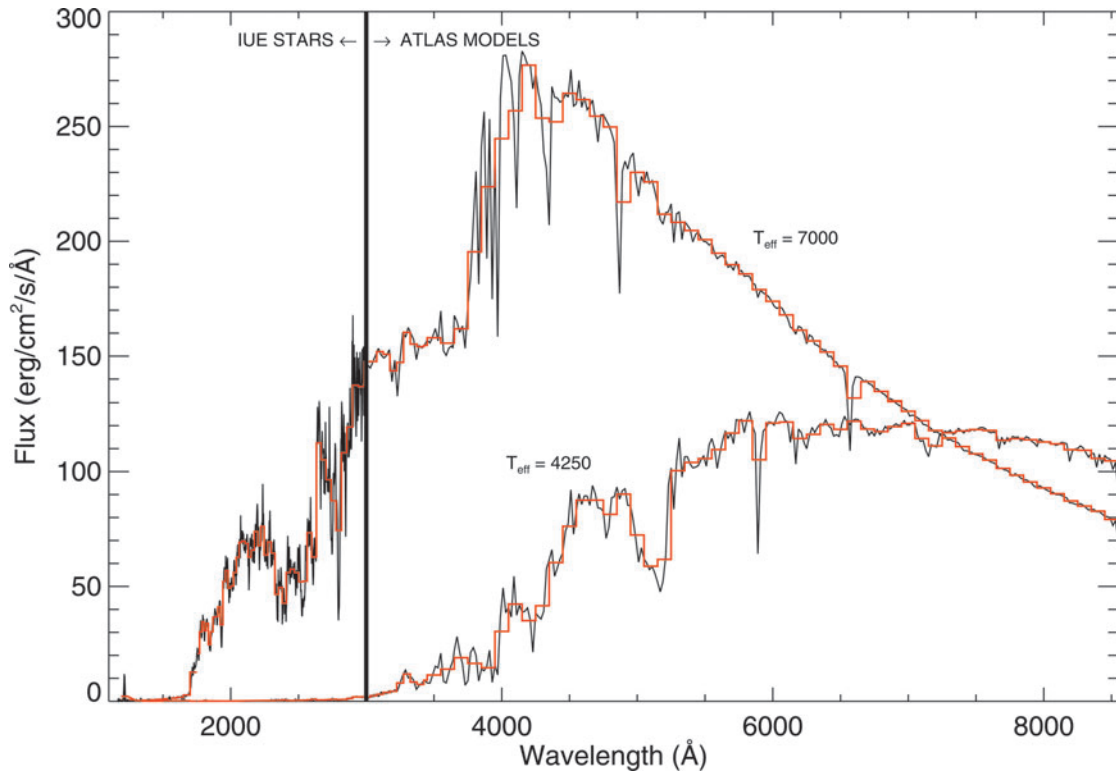
FIG. 1. F0V and K7V composite input stellar spectrum of IUE observations coadded to (black) ATLAS photospheric models (Kurucz, 1979) and (red) binned stellar input. Note: the full input spectrum extends to 45,450 Å. Only the hottest and the coolest star in our grid are shown here for comparison. (Color graphics available online at www.liebertonline.com/ast)

Here, we use a 60% global cloud cover spectrum divided between three layers: 40% water clouds at 1 km, 40% water clouds at 6 km, and 20% ice clouds at 12 km (following Kaltenegger *et al.,* 2007), consistent with an averaged Earth profile to compare our model to this 24 h data set, which should introduce slight discrepancies. To correct the bright-

ness values to match to our full-phase model we use a Lambert phase function.

Our model agrees with EPOXI on an absolute scale within 1–3% for the middle photometric points. The largest discrepancies in the VIS are at 0.45 and 0.95 μm (with an 8% and 18% error, respectively).
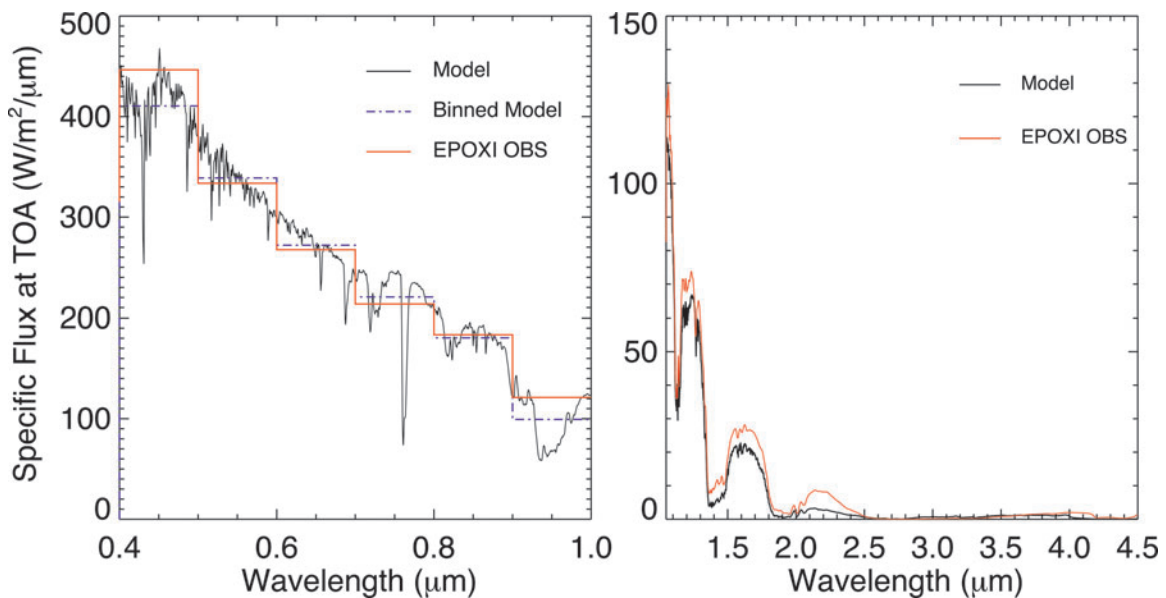

FIG. 2. Comparison of EPOXI data (red) with the Earth model, top-of-atmosphere (TOA) spectrum at full phase from EXO-P (black) in the VIS (left) and near IR (right). (Color graphics available online at www.liebertonline.com/ast)

2.3. Stellar spectral grid model

The stellar spectral grid ranges from 4250 to 7000 K in effective temperature increments of 250 K. This temperature range effectively probes the F0 to K7 main sequence spectral types. For each model star on our grid, we concatenated a solar metallicity, unreddened synthetic ATLAS spectrum, which only considers photospheric emission (Kurucz, 1979), with observations from the International Ultraviolet Explorer (IUE) archive.[1] We use IUE measurements to extend ATLAS synthetic spectra to generate input spectra files from 1150 to 45,450 Å (see Figs. 1 and 2). We choose main sequence stars in the IUE archive with corresponding temperatures close to the grid temperatures and near solar metallicity, as described below.

The IUE satellite had three main cameras, the longwave (LWP/LWR) cameras (1850–3350 Å) and the shortwave (SW) camera (1150–1975 Å). When preparing the IUE data (following Massa et al., 1998; Massa and Fitzpatrick, 2000; Segura et al., 2003), we used a sigma-weighted average to coadd the multiple SW and LW observations. We used a linear interpolation when there were insufficient high-quality measurements to merge the wavelength region from the SW to the LW cameras. IUE measurements were joined to ATLAS model spectra at 3000 Å. In a few cases, a shift factor is needed to match the IUE data to the ATLAS model (see also Segura et al., 2003), but unless stated explicitly, no shift factor was used. Effective temperatures and metallicities are taken from NStED [derived from Flower (1996) and Valenti and Fischer (2005), respectively] unless otherwise cited. See Table 1 for a summary list of the representative IUE stars chosen.

HD 40136, η Lep, is at 15.04 pc with $T_{\rm eff} = 7060$ K and [Fe/H] = −0.13 (Cayrel de Strobel et al., 2001), corresponding to an F0V, the hottest model grid star. Two LW and four SW spectra were coadded and merged with a 7000 K ATLAS spectrum.

To compare with previous work (Selsis, 2000; Segura et al., 2003; Grenfell et al., 2007), we chose HD 128167, σ Boötis, for our model F2V grid star. σ Boötis is an F2V star at 15.47 pc with $T_{\rm eff} = 6730$ K and [Fe/H] = −0.43. Two LW and five SW spectra were coadded and merged with a 6750 K ATLAS spectrum. A slight downward shift of a factor of 0.88 is necessary to match the IUE data with an ATLAS spectrum (see also Segura et al., 2003).

π^3 Orionis, HD 30652, is at 8.03 pc with $T_{\rm eff} = 6450$ K and [Fe/H] = 0.03, corresponding to an F5V grid star. Two LW and three SW spectra were coadded and merged with a 6500 K ATLAS spectrum.

ι Piscium, HD 222368, is at 13.79 pc with $T_{\rm eff} = 6240$ K and [Fe/H] = −0.09, corresponding to an F7V grid star. Two LW and four SW spectra were coadded and merged with a 6250 K ATLAS spectrum.

β Com, HD 114710, is at 9.15 pc with $T_{\rm eff} = 5960$ K and [Fe/H] = 0.07, corresponding to a G0V grid star. Only one LW spectrum was correctable with the Massa routines, and thus one LW and five SW spectra were coadded and merged with a 6000 K ATLAS spectrum.

α Centauri A, HD 128620, is at 1.35 pc with $T_{\rm eff} = 5770$ K and [Fe/H] = 0.21, corresponding to a G2V grid star. Three

Table 1. List of Representative IUE Stars with Their Measured $T_{\rm EFF}$, the $T_{\rm EFF}$ Which Corresponds to Our Grid of Stars, Their Metallicity, and Their Approximate Stellar Type Following Gray (1992)

Star	T_{eff} (K)	T_{eff} (K) grid	[Fe/H]	Spectral type grid
η Lep	7060	7000	−0.13	F0V
σ Boo	6730	6750	−0.43	F2V
π^3 Ori	6450	6500	0.03	F5V
ι Psc	6240	6250	−0.09	F7V
β Com	5960	6000	0.07	F9V/G0V
α Cen A	5770	5750	0.21	G2V
τ Ceti	5500	5500	−0.52	G8V
HD 10780	5260	5250	0.03	K0V
ϵ Eri	5090	5000	−0.03	K2V
ϵ Indi	4730	4750	−0.23	K4V
61 Cyg A	4500	4500	−0.43	K5V
BY Dra	4200	4250	0.00	K7V

LW and 93 SW spectra were coadded and merged with an upward shift of 1.25 to a 5750 K ATLAS spectrum.

τ Ceti, HD 10700, is at 3.65 pc with $T_{\rm eff} = 5500$ K and [Fe/H] = −0.52, corresponding to a G8V grid star. Two LW and eight SW spectra were coadded and merged with a 5500 K ATLAS spectrum.

HD 10780 is at 9.98 pc with $T_{\rm eff} = 5260$ K and [Fe/H] = 0.03, corresponding to a K0V grid star. It is a variable of the BY Draconis type. Five LW and four SW spectra were coadded and merged with a 5250 K ATLAS spectrum.

ϵ Eridani, HD 22049, is at 3.22 pc with $T_{\rm eff} = 5090$ K and [Fe/H] = −0.03, corresponding to a K2V grid star. ϵ Eri was chosen to compare with previous work (Selsis, 2000; Segura et al., 2003; Grenfell et al. 2007). ϵ Eri is a young star, only 0.7 Ga (Di Folco et al., 2004), and is thus more active than a typical K dwarf. Due to its variability and close proximity, there are frequent IUE observations. 17 LW and 72 SW IUE spectra were coadded and merged with a 5000 K ATLAS spectrum.

ϵ Indi, HD 209100, is at 3.63 pc with $T_{\rm eff} = 4730$ K and [Fe/H] = −0.23, corresponding to a K4V grid star. Seven LW and 30 SW IUE spectra were coadded and merged with a 4750 K ATLAS spectrum.

61 Cyg A, HD 201091, is at 3.48 pc with $T_{\rm eff} = 4500$ K and [Fe/H] = −0.43 (Cayrel de Strobel et al., 2001), corresponding to a K5V grid star. 61 Cyg A is a variable star of the BY Draconis type. Six LW and 12 SW spectra were coadded and merged with an upward shift of 1.15 to match the 4500 K ATLAS spectrum.

BY Dra, HD 234677, is at 16.42 pc with $T_{\rm eff} = 4200$ K (Hartmann and Anderson, 1977) and [Fe/H] = 0 (Cayrel de Strobel et al., 1997), corresponding to a K7V grid star. It is a variable of the BY Draconis type. Eight LW and 30 SW spectra were coadded and merged to the 4250 K ATLAS spectrum.

All input stellar spectra are shown in Fig. 3.

2.4. Simulation setup

To examine the effect of the SED of the host star on an Earth-like atmosphere, we built a temperature grid of stellar models ranging from 7000 to 4250 K in steps of 250 K,

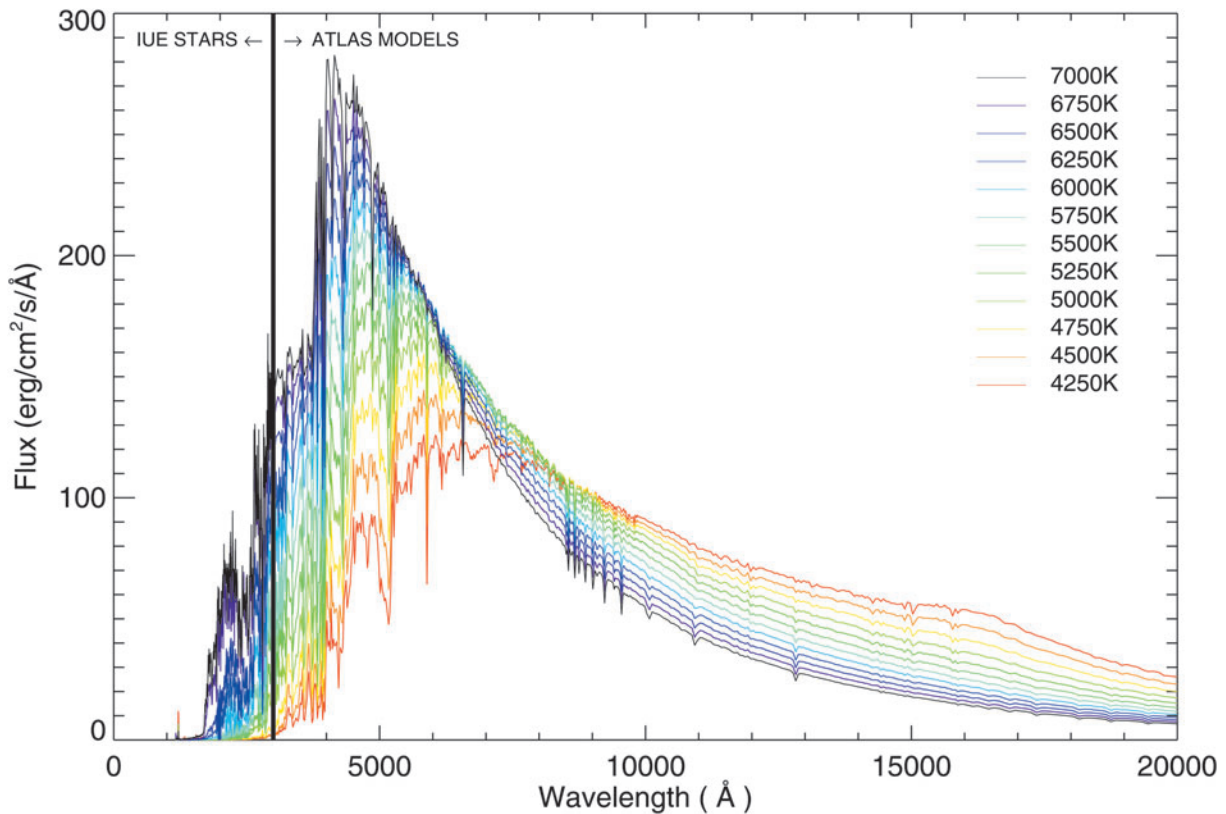**FIG. 3.** Composite stellar input spectra from IUE observations merged to an ATLAS photosphere model at 3000 Å for each grid star. We display up to 20,000 Å here; however, the complete input files extend to 45,450 Å. (Color graphics available online at www.liebertonline.com/ast)

corresponding to F type stars to K dwarfs. We simulated an Earth-like planet with the same mass as Earth at the 1 AU equivalent orbital distance, where the wavelength-integrated stellar flux received on top of the planet's atmosphere is equivalent to 1 AU in our solar system, 1370 W m^{-2}.

The biogenic fluxes were held fixed in the models in accordance with the fluxes that reproduce the modern mixing ratios in the Earth-Sun case (following Segura *et al.*, 2003). We first calculate the surface fluxes for long-lived gases H_2, CH_4, N_2O, CO, and CH_3Cl. Simulating Earth around the Sun with 100 layers yields T_{surf}=288 K for surface mixing ratios: c_{H2}=5.5×10^{-7}, c_{CH4}=1.6×10^{-6}, c_{CO2}=3.5×10^{-4}, c_{N2O}=3.0×10^{-7}, c_{CO}=9.0× 10^{-8}, and c_{CH3Cl}=5.0×10^{-10}. The corresponding surface fluxes are $-1.9×10^{12}$ g H_2/year, $5.3×10^{14}$ g CH_4/year, $7.9×10^{12}$ g N_2O per year, $1.8×10^{15}$ g CO/year, and $4.3×10^{12}$ g CH_3Cl/year. The best estimate for the modern CH_4 flux is $5.35×10^{14}$ g/year (Houghton *et al.*, 1994) and corresponds to the value derived in the model. Fluxes for the other biogenic species are poorly constrained. The N_2 concentration is set by the total surface pressure of 1 bar. To explore the effect of UV and temperature separately, we combine a certain ATLAS model with varying UV files and vice versa.

3. Effect of Stellar SED on Atmospheric Models

The stellar spectrum has two effects on the atmosphere: first, the *UV effect* (Section 3.1) that primarily influences photochemistry and second, the *temperature effect* (Section 3.2) resulting from the difference in absorbed flux as a

function of stellar SED. The same planet has a higher Bond albedo around hotter stars with SEDs peaking at shorter λ, where Rayleigh scattering is more efficient, than it would have around cooler stars, assuming the same total stellar flux (Sneep and Ubachs, 2004). The overall resulting planetary Bond albedo that includes both atmospheric as well as surface albedo is calculated by the climate/photochemistry model and varies between 0.13 and 0.22 for planets around

TABLE 2. SURFACE TEMPERATURE AND O$_3$ COLUMN DEPTH FOR AN EARTH-LIKE PLANET MODEL ORBITING THE GRID STARS

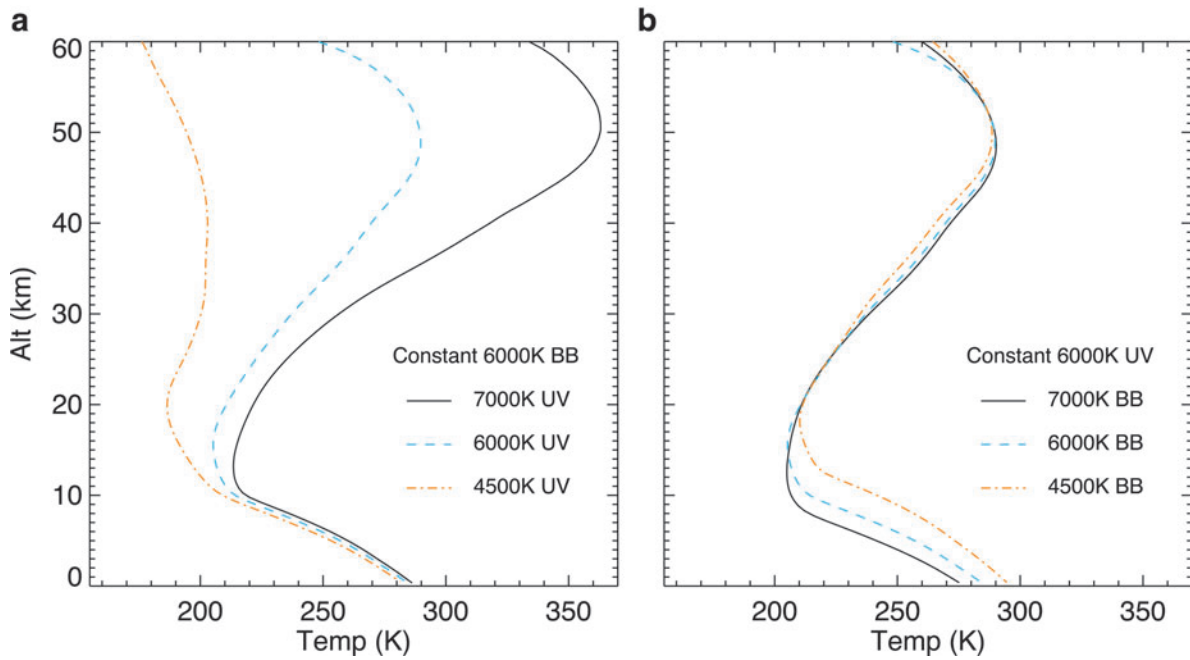| T_{eff} (K) grid	Spectral type grid	Surface temperature (K)	Ozone column depth (cm^{-2})
7000	F0V	279.9	1.2×10^{19}
6750	F2V	281.7	1.1×10^{19}
6500	F5V	283.2	9.6×10^{18}
6250	F7V	284.6	8.3×10^{18}
6000	F9V/G0V	286.4	7.3×10^{18}
SUN	G2V	288.1	5.3×10^{18}
5750	G2V	287.7	5.1×10^{18}
5500	G8V	289.1	3.2×10^{18}
5250	K0V	290.9	4.1×10^{18}
5000	K2V	291.9	3.3×10^{18}
4750	K4V	292.8	2.6×10^{18}
4500	K5V	297.0	2.6×10^{18}
4250	K7V	300.0	3.5×10^{18}

FIG. 4. Temperature/altitude profiles for several unphysical tests where we (**a**) combine high, mid, and low UV fluxes (IUE observations for stars with $T_{eff} = 7000$, 6000, and 4500 K, respectively) with a fixed ATLAS photosphere model for $T_{eff} = 6000$ K to show the "UV effect" and (**b**) combine high, mid, and low stellar photosphere models (ATLAS models for $T_{eff} = 7000$, 6000, and 4500 K, respectively) with a fixed UV flux for $T_{eff} = 6000$ K to show the "temperature effect." (Color graphics available online at www.liebertonline.com/ast)
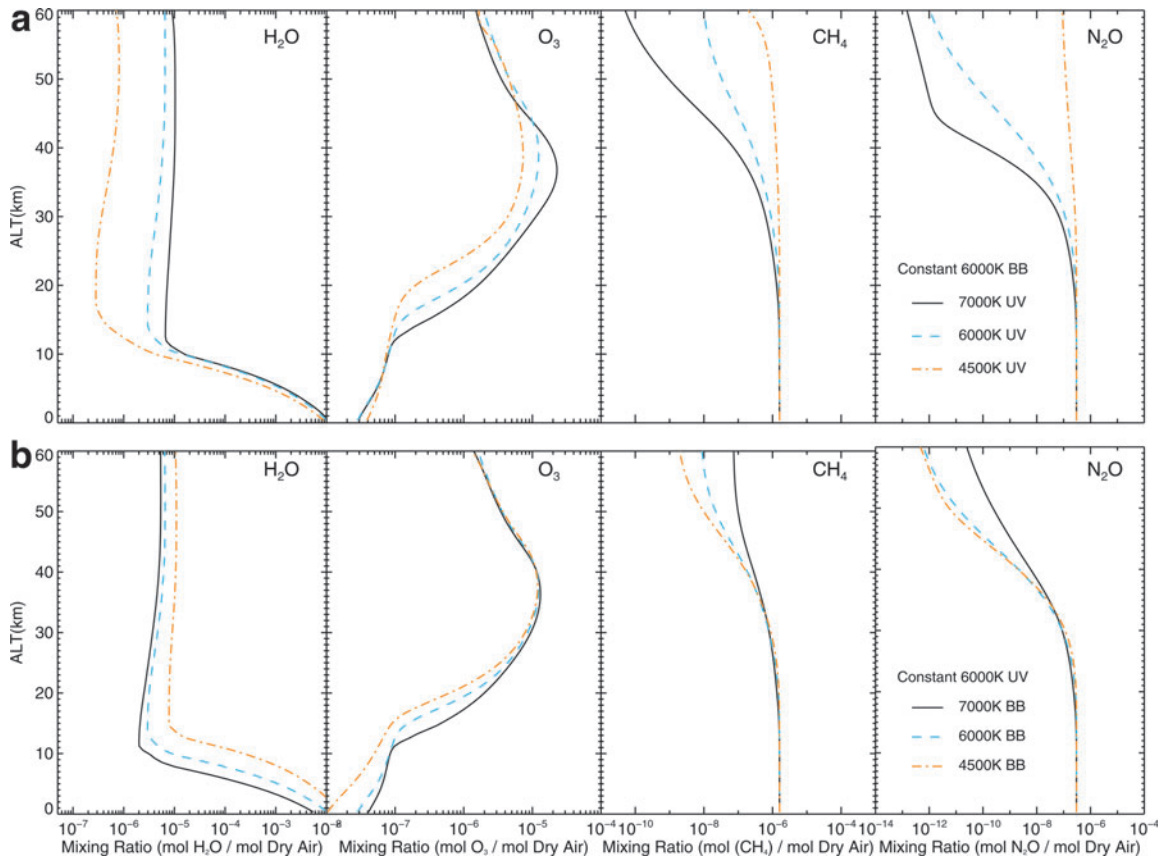
FIG. 5. Chemical mixing ratio profiles for H_2O, O_3, CH_4, and N_2O from several unphysical tests where we (**a**) combine high, mid, and low UV fluxes (IUE observations for stars with $T_{eff} = 7000$, 6000, and 4500 K, respectively) with a fixed ATLAS photosphere model for $T_{eff} = 6000$ K to show the "UV effect" and (**b**) combine high, mid, and low stellar photosphere models (ATLAS models for $T_{eff} = 7000$, 6000, and 4500 K, respectively) with a fixed UV flux for $T_{eff} = 6000$ K to show the "temperature effect." (Color graphics available online at www.liebertonline.com/ast)
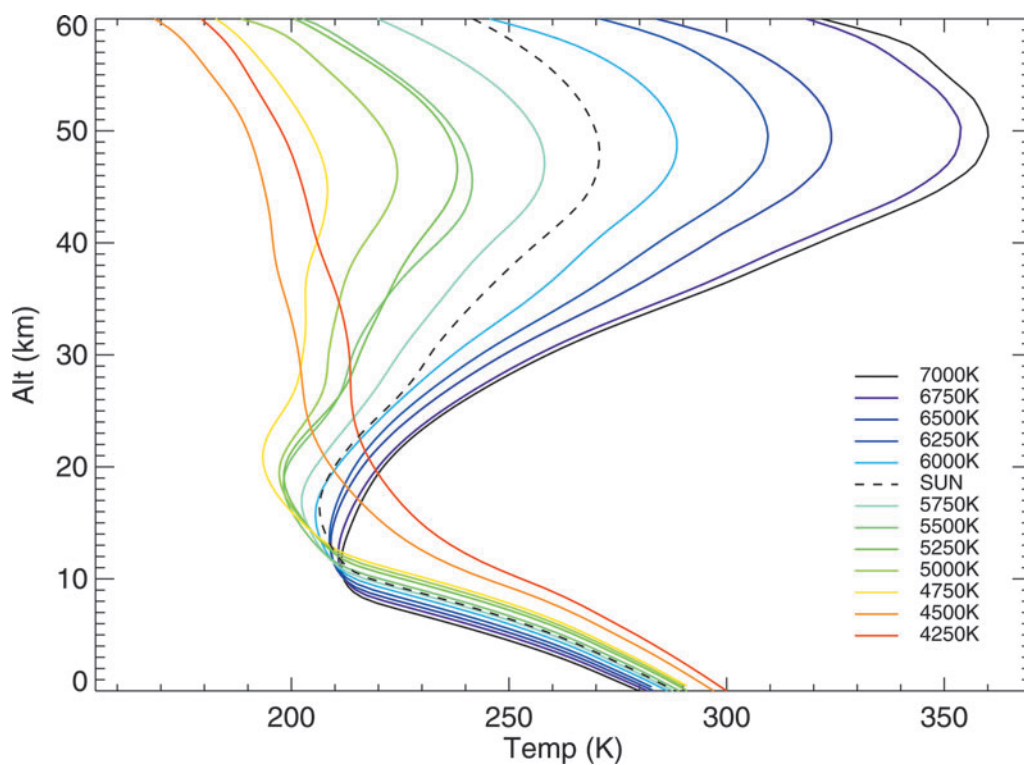
FIG. 6. Planetary temperature/altitude profiles for different stellar types showing the combined temperature and UV effect. (Color graphics available online at www.liebertonline.com/ast)
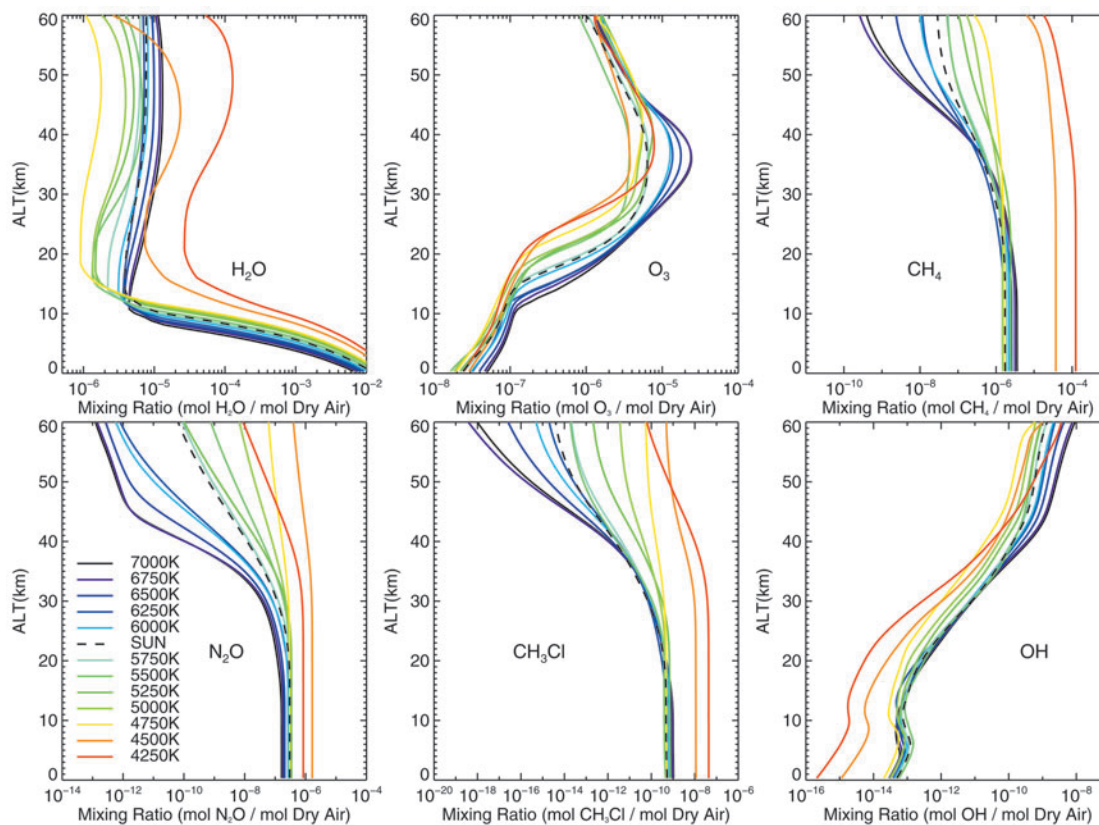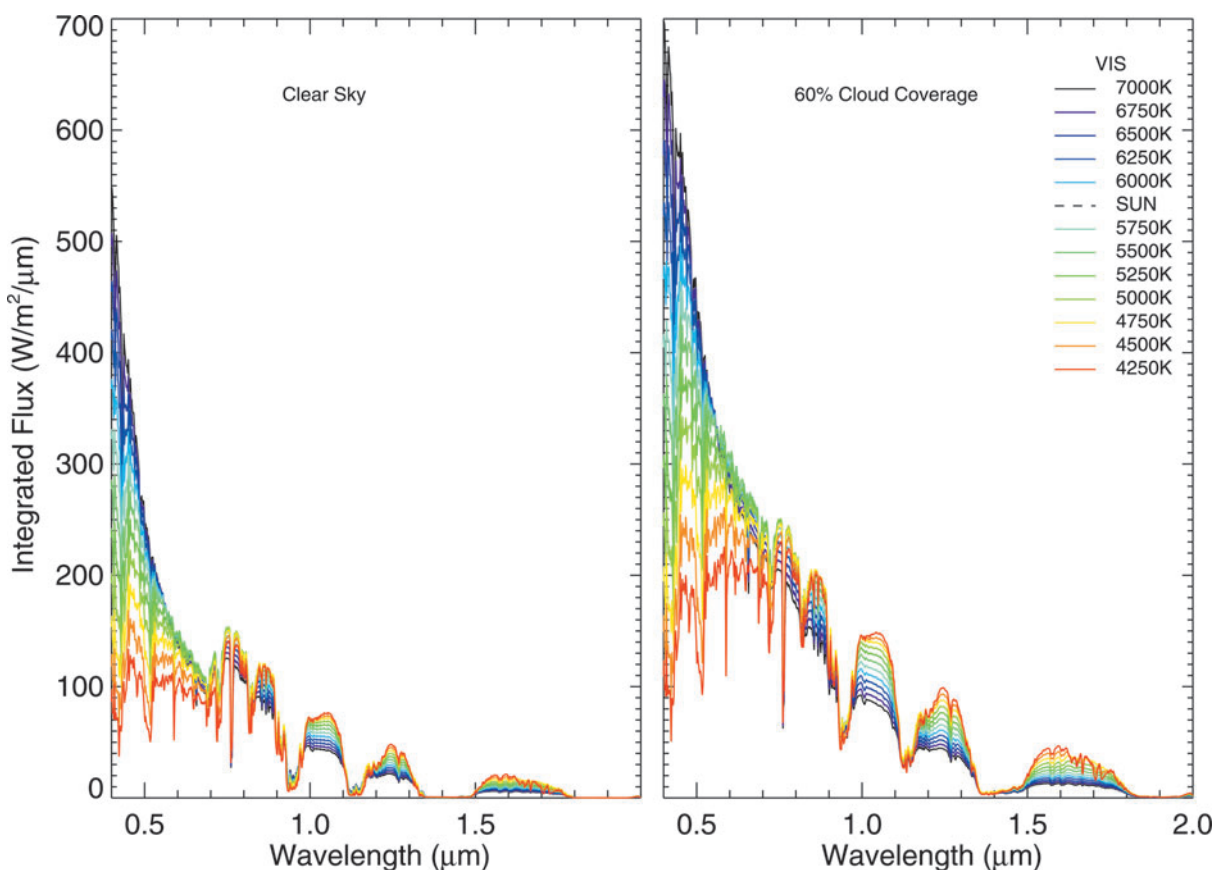

FIG. 7. Photochemical model results for the mixing ratios of the major molecules H_2O, O_3, CH_4, N_2O, CH_3Cl, and OH for each stellar spectral type in our grid of stars showing the combined temperature and UV effect. (Color graphics available online at www.liebertonline.com/ast)

FIG. 8. Smoothed, disk-integrated VIS/NIR spectra at the TOA for an Earth-like planet around FGK stars for both a clear sky (left) and 60% cloud coverage (right) model (region 2–4 μm has low integrated flux levels and therefore is not shown here). (Color graphics available online at www.liebertonline.com/ast)

F0 stars to K7 stars, respectively, because of the stars' SED. Note that these values are lower than Earth's planetary Bond albedo of 0.31 because the warming effect of clouds is folded into the albedo value in the climate code, decreasing it artificially.

3.1. The influence of UV levels on Earth-like atmosphere models (UV effect)

To explore the effects of UV flux alone on the atmospheric abundance of different molecules, we combined specific IUE data files for stars with T_{eff}=7000, 6000, and 4500 K (representing high, mid, and low UV flux) with a fixed ATLAS photosphere model of T_{eff}=6000 K. The temperature/pressure and chemical profiles of this test are shown in panels (a) of Figs. 4 and 5. Hot stars provide high UV flux in the 2000–3200 Å range; for example, an F0V grid star emits 130×more flux in this wavelength range than a K7V grid star (Figs. 1 and 2).

The Chapman reactions are driven primarily by photolysis in this wavelength range, and the atmospheric models show an according increase in O_3 concentration and subsequent strong temperature inversion for planets orbiting hot grid stars (Table 2). The maximum heating in the stratosphere is a few kilometers above the peak of the O_3 concentration where both a high enough concentration of O_3 and a high enough flux of photons is present. O_3 abundance increases OH abundance, the primary sink of CH_4 and CH_3Cl. Figs. 5 and 7 show a corresponding decrease in those molecules for

high-UV environment. O_3 shields H_2O in the troposphere from UV environments. Stratospheric H_2O is photolyzed by $\lambda < 2000$ Å or reacts with excited oxygen, $O(^1D)$, to produce OH radicals. Accordingly, stratospheric H_2O concentration decreases with decreasing UV flux. N_2O decreases with increasing UV flux because of photolysis by $\lambda < 2200$ Å. N_2O is also an indirect sink for stratospheric O_3 when it is converted to NO. Therefore, decreasing N_2O increases O_3 abundance. O_2 and CO_2 concentrations remain constant and well mixed for all stellar types.

3.2. The influence of stellar T_{eff} on Earth-like atmosphere models (temperature effect)

To explore the effects of stellar T_{eff} alone on the atmospheric abundance of different molecules, we combined specific photospheric ATLAS spectrum of T_{eff}=7000, 6000, and 4500 K (representing high, mid, and low stellar T_{eff}) with a fixed UV data file of T_{eff}=6000 K. The temperature/pressure and chemical profiles of this test are shown in panels (b) of Figs. 4 and 5. T_{eff} affects H_2O vapor concentrations due to increased evaporation for high planetary surface temperature, which is transported to the stratosphere. Figure 4 shows an overall increase in tropopause and stratopause height for low stellar T_{eff} with corresponding hot planetary surface temperatures.

The response of O_3 to stellar T_{eff} is weak due to two opposing effects: high stellar T_{eff} and corresponding low
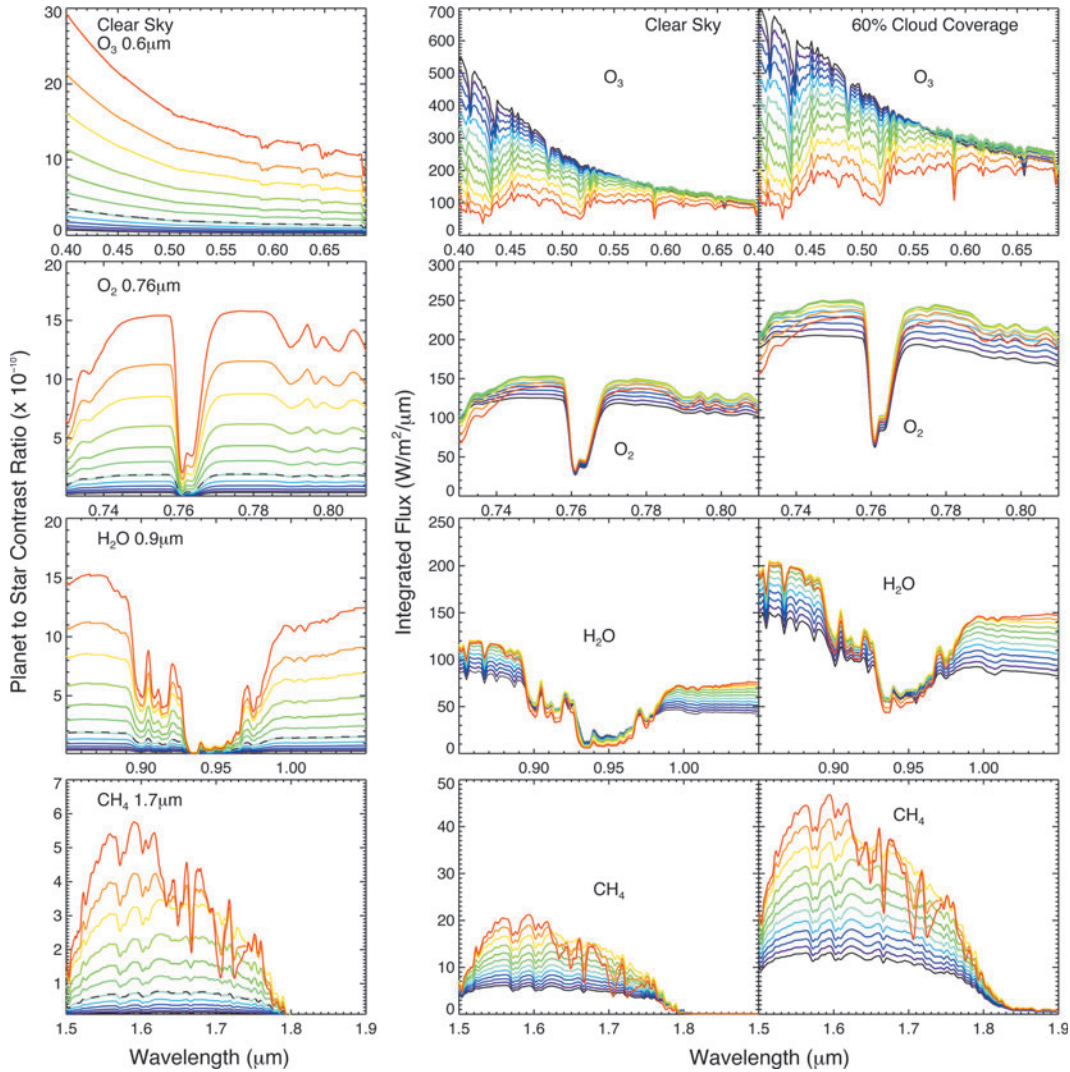
FIG. 9. Individual features of O_3 at 0.6 μm, O_2 at 0.76 μm, H_2O at 0.95 μm, and CH_4 at 1.7 μm for F0V–K7V grid stars (left) planet-to-star contrast ratio and absolute flux levels (middle) for a clear sky and (right) 60% cloud coverage model. Note the different y axes. Legend and color coding are the same in Figs. 6–11. (Color graphics available online at www.liebertonline.com/ast)

planetary surface and atmospheric temperatures increase O_3 concentration by slowing Chapman reactions that destroy O_3, but also increase NO_x, HO_x, and ClO_x concentrations, which are the primary sinks of O_3 (see also Grenfell *et al.*, 2007).

Both CH_4 and CH_3Cl show only a weak temperature dependence. The rate of the primary reactions of CH_4 and CH_3Cl with OH slows with decreasing temperature, causing an increase in CH_4 and CH_3Cl for lower planetary surface temperatures. N_2O displays a similar weak temperature effect.

All our simulations used a fixed mixing ratio of 355 ppm for CO_2 and 21% O_2. Since both O_2 and CO_2 are well mixed in the atmosphere, their vertical mixing ratio profiles are not shown.

3.3. The influence of stellar SED on Earth-like atmosphere models

Figures 6 and 7 show the combined temperature and UV effect on Earth-like atmospheres. The surface temperature of

an Earth-like planet increases with decreasing stellar effective temperature due to decreasing reflected stellar radiation and increasing IR absorption by H_2O and CO_2 (see Table 2 and Fig. 6). The late K dwarf stars show in addition a near isothermal stratosphere.

Figure 7 shows the corresponding atmospheric mixing ratios versus height for the grid stars. The top height considered in our atmospheric models is 60 km for a Sun-like star, which corresponds to 10^{-4} bar (following Segura *et al.*, 2003). For hotter stars, the stratosphere is warmer, which increases the pressure at 60 km to 4.0×10^{-4} bar, while for cooler stars the pressure at 60 km decreases to 3.0×10^{-5} bar.

Earth-like atmosphere models around hot grid stars show high O_3 concentration (see Table 2) and therefore strong temperature inversions due to the increased stellar UV flux (Fig. 6). Cooler stars often have stronger emission lines and higher activity. Accordingly, the two coldest grid stars in our sample ($T_{eff} = 4250$ K and 4500 K) show a large O_3 abundance due to high stellar Ly α flux. In fact, the UV output of the coldest grid star, $T_{eff} = 4250$ K, is almost $2 \times$ the
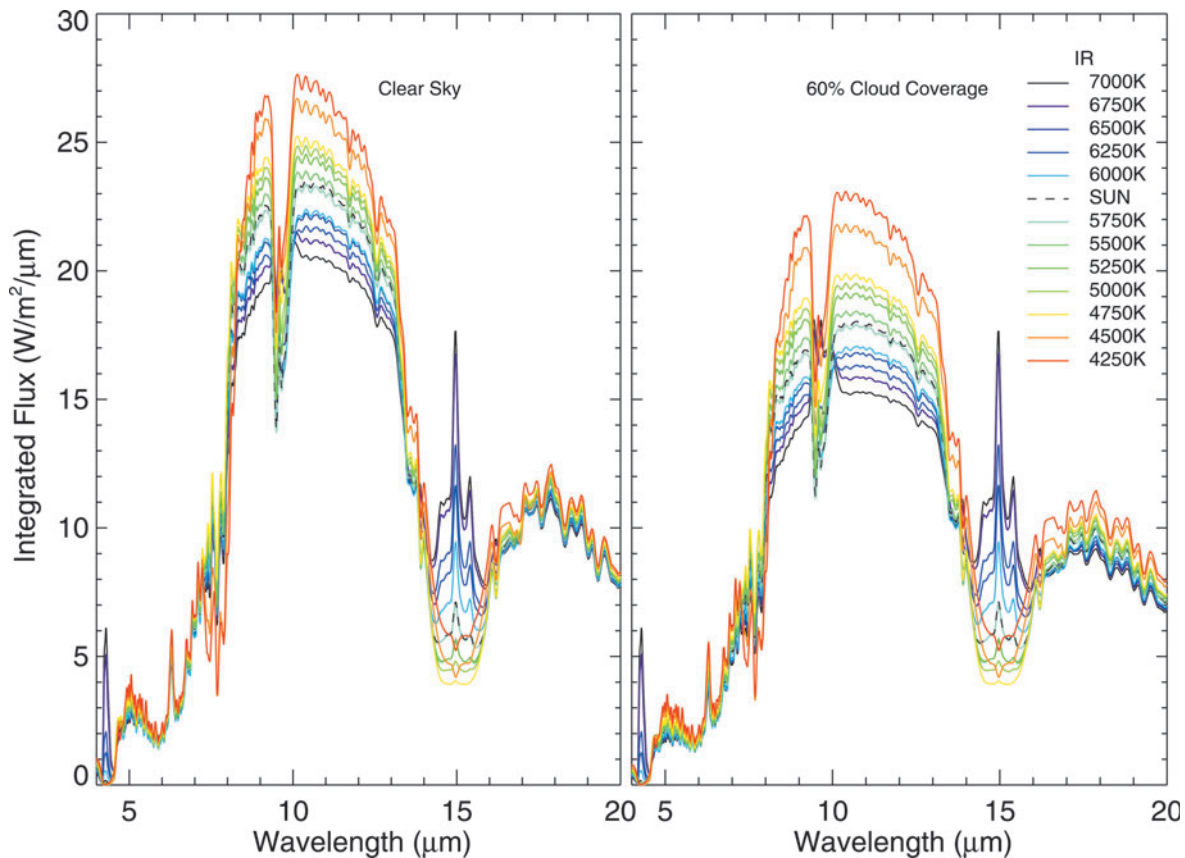
FIG. 10. Smoothed, disk-integrated IR spectra at the TOA for Earth-like planets around F0V–K7V grid stars for both a clear sky (left) and 60% cloud coverage (right) model. (Color graphics available online at www.liebertonline.com/ast)

UV flux of the second coldest grid star, $T_{eff} = 4500$ K, also due to its younger age. Thus, there is more O_3 produced for the coldest star. However, in the 2000–3000 Å wavelength region these cold grid stars emit low UV flux and therefore produce near isothermal stratospheres (see also M dwarf models of Segura et al., 2005). The detailed effect of Ly α flux on the planet's atmosphere will be modeled in a future study.

Earth-like atmosphere models around hot grid stars also show high OH concentrations due to a higher availability of high-energy photons, as well as O_3 and H_2O molecules (Fig. 7). Cold grid stars ($T_{eff} = 4250$ K) show higher OH concentration in the stratosphere than expected from an extrapolation from the other grid stars due to the increased O_3 and H_2O concentrations at those altitudes.

CH_4 abundance increases with decreasing stellar temperature, dominated by the effects of decreasing stellar UV. Stratospheric CH_4 decreases in atmospheric models around hot grid stars since both OH concentration and UV flux increase with stellar T_{eff} and act as sinks of CH_4.

H_2O abundance in the troposphere is dominated by the surface temperature of the planet. Earth-like planet atmosphere models around cool grid stars generate warmer planetary surface temperatures and therefore high amounts of tropospheric H_2O. High UV flux generally decreases H_2O concentration in the stratosphere through photolysis, but increased O_3 concentrations provide shielding from the photolysis of H_2O. Also, cold grid stars ($T_{eff} = 4250$ K and 4500 K) show increased stratospheric H_2O concentration

through increased vertical transport in the nearly isothermal stratospheres as well as production by stratospheric CH_4 [see, e.g., Segura et al. (2005) for similar behavior in planets around M dwarfs]. In particular, the atmospheric models for a planet around a $T_{eff} = 4250$ K grid star have a high OH concentration in the stratosphere due to increased O_3 and H_2O at those altitudes.

N_2O is primarily produced by denitrifying bacteria and has increased linearly due to agriculture since the preindustrial era at a rate of around 0.26% year^{-1} (Forster et al., 2007). Up to about 20 km, there is no significant difference between stellar types in N_2O concentration. Figure 7 shows that above ∼20 km a decrease in N_2O concentration occurs for atmospheric models of planets around hot grid stars but does not occur for those of cool grid stars, since UV is the primary sink of N_2O in the stratosphere. Below 20 km, N_2O is shielded from photolysis by the O_3 layer. Note that the general trend for increasing N_2O for colder grid stars reverses for our coldest grid star. This is due to the increased UV flux, which destroys N_2O, and an increase in O_3, which causes an increase in $O(^1D)$, another strong sink for N_2O.

CH_3Cl concentration decreases with increased stellar UV flux since OH acts as a sink for CH_3Cl.

4. Results: Spectra of Earth-like Planets Orbiting F0V to K7V Grid Stars

We include both a clear sky as well as a 60% global cloud cover spectrum that has cloud layers analogous to Earth
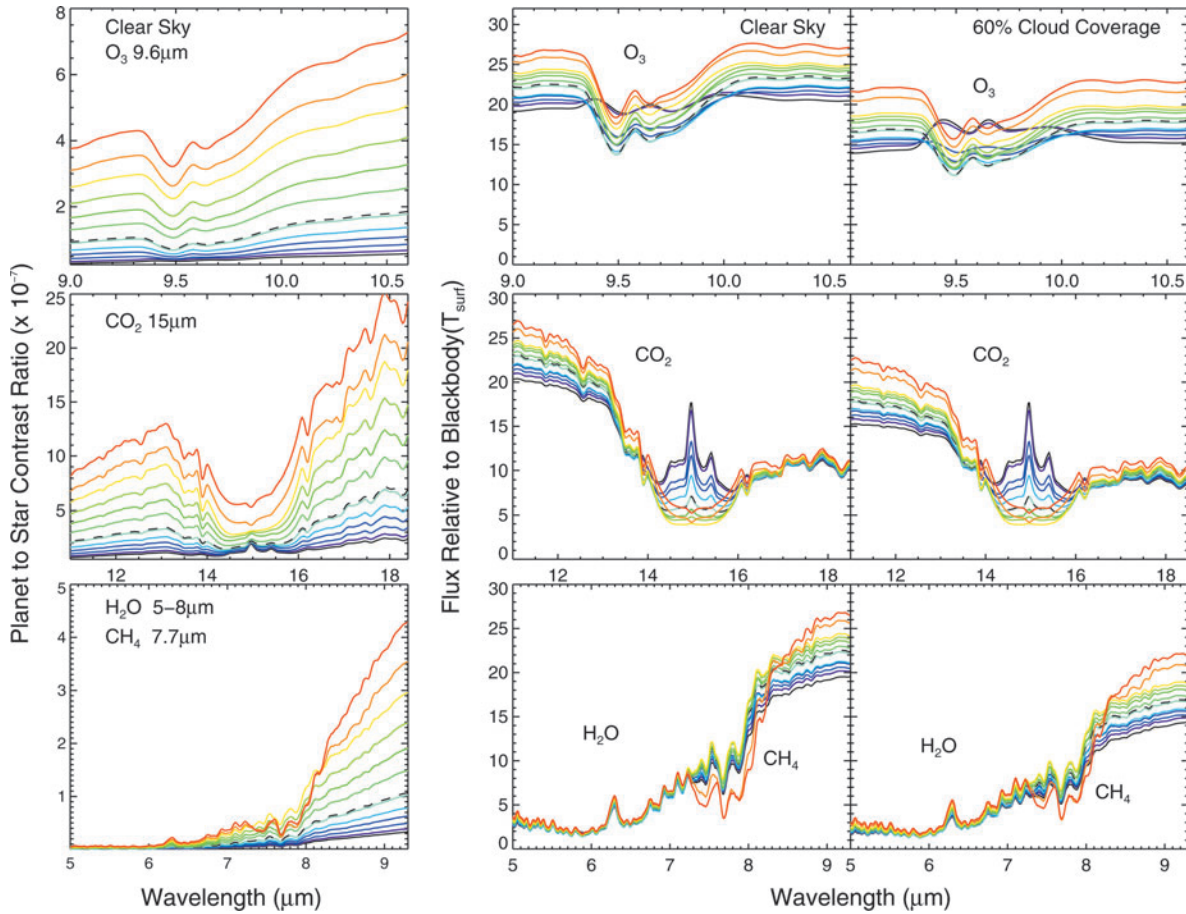
FIG. 11. Individual features of O_3 at 9.6 μm, CO_2 at 15 μm, H_2O at 5–8 μm, and CH_4 at 7.7 μm for F0V–K7V grid stars (left) planet-to-star contrast ratio and absolute flux levels (middle) for a clear sky and (right) 60% cloud coverage model. Legend and color coding are the same in Figs. 2–8. (Color graphics available online at www.liebertonline.com/ast)

[40% 1 km, 40% 6 km, and 20% 12 km following Kaltenegger *et al.* (2007)] in Figs. 8–11 to show the importance of clouds on the reflected and emission planet spectra. We present the spectra as specific flux at the top of the atmosphere of Earth-like planets. In the VIS, the depth of the absorption features is primarily sensitive to the abundance of the species, while in the IR, both the abundance and the temperature difference between the emitting/absorbing layer and the continuum influence the depth of features.

We use a Lambert sphere as an approximation for the disk-integrated planet in our model. The surface of our model planet corresponds to Earth's current surface of 70% ocean, 2% coast, and 28% land. The land surface consists of 30% grass, 30% trees, 9% granite, 9% basalt, 15% snow, and 7% sand. Surface reflectivities are taken from the USGS Digital Spectral Library[2] and the ASTER Spectral Library[3] (following Kaltenegger *et al.*, 2007). Note the vegetation red edge feature at 0.76 μm is only detectable in the clear sky model spectra in low resolution; see Fig. 8 (see, *e.g.*, Kaltenegger *et al.*, 2007; Seager *et al.*, 2005; Pallé *et al.*, 2008). No noise has been added to these model spectra to provide input

models for a wide variety of instrument simulators for both secondary eclipse and direct detection simulations.

We assume full phase (secondary eclipse) for all spectra presented to show the maximum flux that can be observed. Note that we use an Earth-sized planet to determine the specific flux and planet-to-star contrast ratio. A Super-Earth with up to twice Earth's radius will provide up to 4×more flux and a better contrast ratio than shown in Figs. 8–12.

4.1. Earth-like VIS/near-IR spectra (0.4 to 4 μm)

Figure 8 shows spectra from 0.4 to 2 μm of Earth-like planets for both a clear-sky and Earth-analog cloud cover for the grid stars (F0V–K7V). The high-resolution spectra have been smoothed to a resolving power of 800 with a triangular smoothing kernel. Figures 8 and 9 show that clouds increase the reflectivity of an Earth-like planet in the VIS to near IR substantially and therefore overall increase the equivalent width of all observable features, even though they block access to some of the lower atmosphere.

Figure 9 shows individual features for the strongest atmospheric features from 0.4 to 4 μm for Earth-like planets orbiting the grid stars: O_3 at 0.6 μm (the Chappuis band), O_2 at 0.76 μm, H_2O at 0.95 μm, and CH_4 at 1.7 μm. The left panel of each row shows the relative flux as planet-to-star contrast ratio; the middle and right panel show the specific,
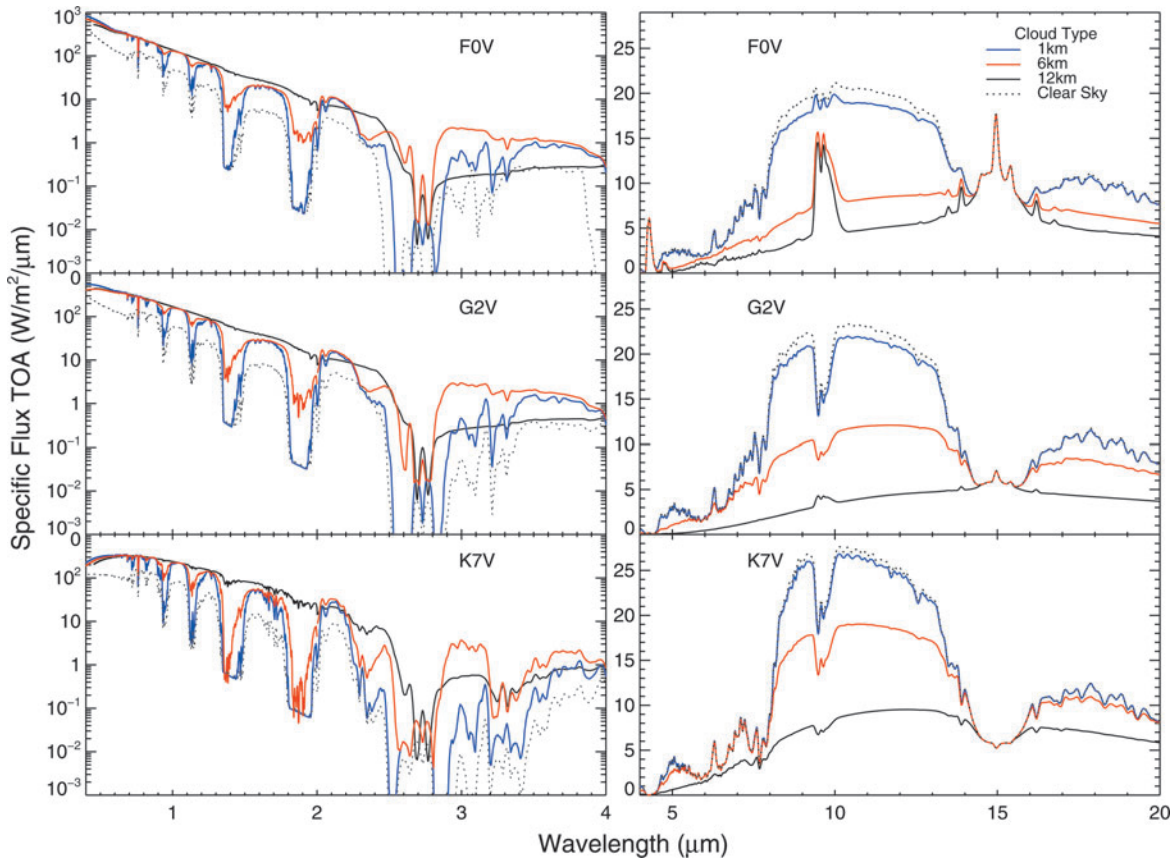
FIG. 12. Spectra of Earth-like planets for 100% cloud coverage at three cloud heights (1, 6, and 12 km, blue, red, and black line, respectively) as well as clear sky spectrum (dashed line) from 0.4 to 20 μm, orbiting a $T_{eff} = 7000$ K (top) $T_{eff} = 5750$ K (middle), and $T_{eff} = 4250$ K (bottom) grid star for comparison. (Color graphics available online at www.liebertonline.com/ast)

top-of-atmosphere (TOA) flux for a clear and 60% cloud cover, respectively. From the planet-to-star contrast ratios in Figs. 9, 11, and 13, the photometric precision required to detect these features for Earth-like planets can be calculated. Note that any shallow spectral features like the visible O_3 feature would require a very high signal-to-noise ratio to be detected.

The 0.6 μm shallow O_3 spectral feature depth increases with T_{eff} of the host star since O_3 concentration increases with UV levels but is difficult to distinguish from Rayleigh scattering. The relative depth of the O_2 feature at 0.76 μm is constant, but the detectable flux decreases for cool grid stars due to the decrease in absolute stellar flux received and reflected by the planet at short wavelengths. The depth of the H_2O absorption feature at 0.9 μm (shown) 0.8, 1.1, and 1.4 μm increases for planets orbiting cool grid stars due to their increased H_2O abundance. The depth of the CH_4 absorption feature at 1.7 μm increases with decreasing stellar T_{eff} due to the increase of CH_4 abundance.

From 2 to 4 μm, there are CH_4 features at 2.3 and 3.3 μm, a CO_2 feature at 2.7 μm, and H_2O absorption at 2.7 and 3.7 μm. However, due to the low emergent detectable flux in this region, these features are not shown individually.

4.2. Earth-like IR spectra, IR (4 to 20 μm)

Figure 10 shows spectra from 4 to 20 μm of Earth-like planets for both a clear sky and Earth-analog cloud cover for the grid stars (F0V–K7V). The high-resolution spectra have been smoothed to a resolving power of 250 with a triangular smoothing kernel. Clouds decrease the overall emitted flux of an Earth-like planet in the IR.

Figure 11 shows individual features for the strongest atmospheric features from 4 to 20 μm for Earth-like planets orbiting the grid stars: O_3 at 9.6 μm, CO_2 at 15 μm, H_2O at 6.3 μm, and CH_4 at 7.7 μm for a cloud-free and Earth-analog cloud coverage model. The left panel of each row shows the relative flux as planet-to-star contrast ratio; the middle and right panel show the specific, TOA flux for a clear and 60% cloud coverage case, respectively.

In the clear sky model, the depth of the O_3 feature at 9.6 μm decreases for planetary models orbiting hot grid stars, despite increasing O_3 abundance, due to lower contrast between the continuum and absorption layer temperature. For Earth-analog cloud cover, however, O_3 is seen in emission for $T_{eff} \geq 6500$ K due to the lower continuum temperature.

Due to the hot stratosphere for all grid stars with $T_{eff} > 6000$ K, the CO_2 absorption feature at 15 μm has a prominent central emission peak. Clouds reduce the continuum level and the depth of the observable CO_2 feature.

The CH_4 feature at 7.7 μm is prominent in the planetary spectra around cool grid stars due to high CH_4 abundance in low-UV environments. The CH_4 feature is also partially obscured by the wings of the H_2O feature at 5–8 μm. The depth of the H_2O features at 5–8 and 18+ μm does not change
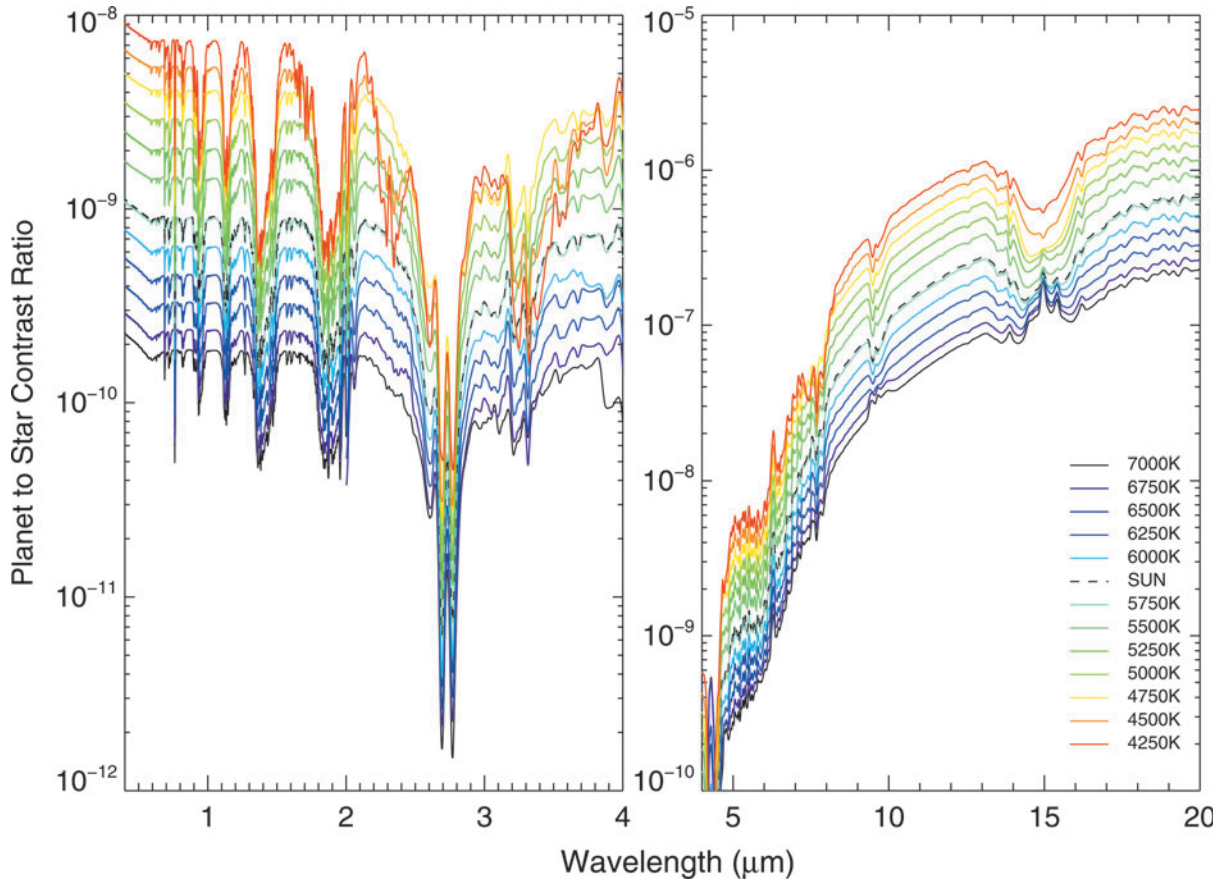
FIG. 13. Contrast ratio of Earth-like planets for Earth-analog cloud coverage. (Color graphics available online at www.liebertonline.com/ast)

significantly even though H_2O abundance increases for cool grid stars. Clouds reduce the continuum level and the depth of the observable H_2O features.

Figure 13 shows planet-to-star contrast ratio for Earth-analog cloud cover of an Earth-like planet from which the photometric precision required can be calculated. The planet-to-star contrast ratio is between 10^{-8} and 10^{-11} in the VIS/near IR and between about 10^{-6} and 10^{-10} in the IR for the grid stars. For the whole wavelength range, the contrast ratio improves for cool grid stars.

4.3. The effect of clouds on Earth-like planet spectra from 0.4 to 20 μm

Figure 12 shows Earth-like planet spectra for 100% cloud cover at 1, 6, and 12 km from 0.4 to 20 μm for three sample grid stars with $T_{eff} = 7000$ K (top), 5750 K (middle), and 4250 K (bottom). The clear sky spectrum is shown as a dashed line for comparison. Clouds increase the reflectivity of an Earth-like planet in the VIS to near IR substantially and therefore overall increase the equivalent width of all observable features, even though they block access to some of the lower atmosphere. Clouds decrease the overall emitted flux of an Earth-like planet in the IR slightly because they radiate at lower temperatures and therefore overall decrease the equivalent width of all observable absorption features, even though they can increase the relative depth of a spectral

feature due to lowering the continuum temperature of the planet.

Figure 14 shows the individual chemical absorption features as discussed in Sections 4.1 and 4.2 on a relative scale for H_2O, CO_2, O_2, O_3, CH_4, N_2O, and CH_3Cl from 0.4 to 20 μm to complement the spectra, shown in Figs. 5–9, that focus on the remote detectability of individual features for future space missions.

5. Discussion

When choosing IUE stars for our stellar spectral grid, we avoided stars of unusual variability but did not exclude stars that had representative variability of its stellar class. Several of our representative K stars are variables of the BY Draconis type, which is a common variable in this stellar type. We preferentially chose stars with near solar metallicity when possible; however, the IUE database does not provide candidate stars at each temperature of solar metallicity. Several stars have lower than solar metallicity. We compared a subsolar stellar metallicity with a solar metallicity spectra model and found that the difference does not impact our results.

Observability of biosignatures: Detecting the combination of O_2 or O_3 and CH_4 for emergent spectra and secondary eclipse measurements requires observations in the IR or in the VIS/near IR up to 3 μm to include the 2.4 μm
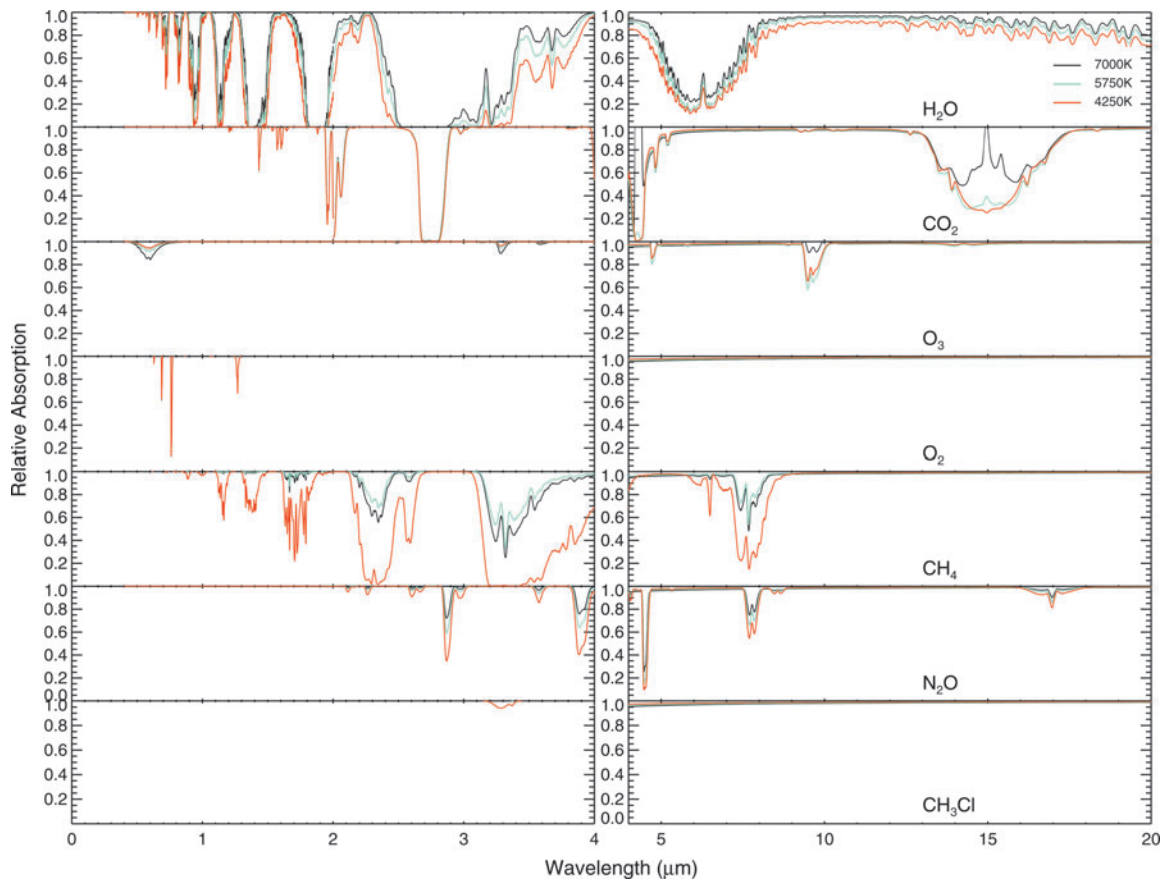
FIG. 14. Relative absorption of individual chemical species H_2O, CO_2, O_3, O_2, CH_4, N_2O, and CH_3Cl for three sample grid stars with $T_{eff} = 7000$, 5750, and 4250 K. (Color graphics available online at www.liebertonline.com/ast)

CH_4 feature in that spectral range. The strength of the absorption features depends on the stellar effective temperature of the host star and varies significantly between stellar types. In the IR, CH_4 at 7.7 μm is more detectable at low resolution for cool grid stars than hot grid stars. The 9.6 μm O_3 feature is deepest for mid to cool stars and becomes less detectable for hotter stars. However, around our hottest grid stars, the 9.6 μm O_3 feature becomes an apparent emission feature for cloudy atmospheres. The narrow O_2 feature in the VIS at 0.72 μm is of comparable strength for all grid stars. H_2O has strong features for all grid stars over the whole wavelength range.

N_2O and CH_3Cl have features from the near IR to IR (see Fig. 14) but in modern Earth concentrations do not have a strong enough feature to be detected with low resolution. For the clear sky models, the vegetation red edge is detectable due to the order of magnitude increased reflectance from 0.7 to 0.75 μm for all grid stars. Clouds obscure that feature (see Fig. 8).

For detecting an oxidizing gas in combination with a reducing gas in Earth-like planet atmosphere models, the coolest grid stars in our sample are the best targets. In this study, we did not model planets orbiting stars cooler than ~4000 K to provide a consistent set of planetary models. As discussed by Segura *et al.* (2005), cool host stars with low UV flux provide an environment that leads to runaway CH_4 accumulation in the atmosphere; therefore the model for Earth-like planets around M dwarfs often uses abiotic CH_4

levels, which is not consistent with Earth-analog models used in this study. We will explore this effect in future work.

No noise has been added to these model spectra to provide input models for a wide variety of instrument simulators for both secondary eclipse and direct detection simulations. Different instrument simulators for JWST (see, *e.g.*, Deming *et al.*, 2009; Kaltenegger and Traub, 2009) explore the capability of JWST's MIRI and NIRspec Instrument to characterize extrasolar planets down to Earth-like planets, with interesting results for planets around close-by as well as luminous host stars. Several new results are forthcoming by several groups that will provide realistic instrument parameters that can be used to determine detectability of these absorption features. Future ground- and space-based telescopes are being designed to characterize exoplanets down to Earth-like planets and will provide interesting opportunities to observe atmospheric features, especially for super-Earths, with radii up to 2 × Earth's radius and therefore up to 4 × the flux and planet-to-star contrast ratio levels quoted for Earth-sized planets shown in Figs. 8–14.

In addition to the size of the planet, future observations will occur at different positions throughout the planet's orbit. The maximum observable planetary flux in the VIS scales with the illuminated fraction of the planet that is "visible" to the observer. In the IR, the maximum flux remains constant throughout the planet's orbit, assuming a similar temperature on the dayside and nightside. In Fig. 15, we show the
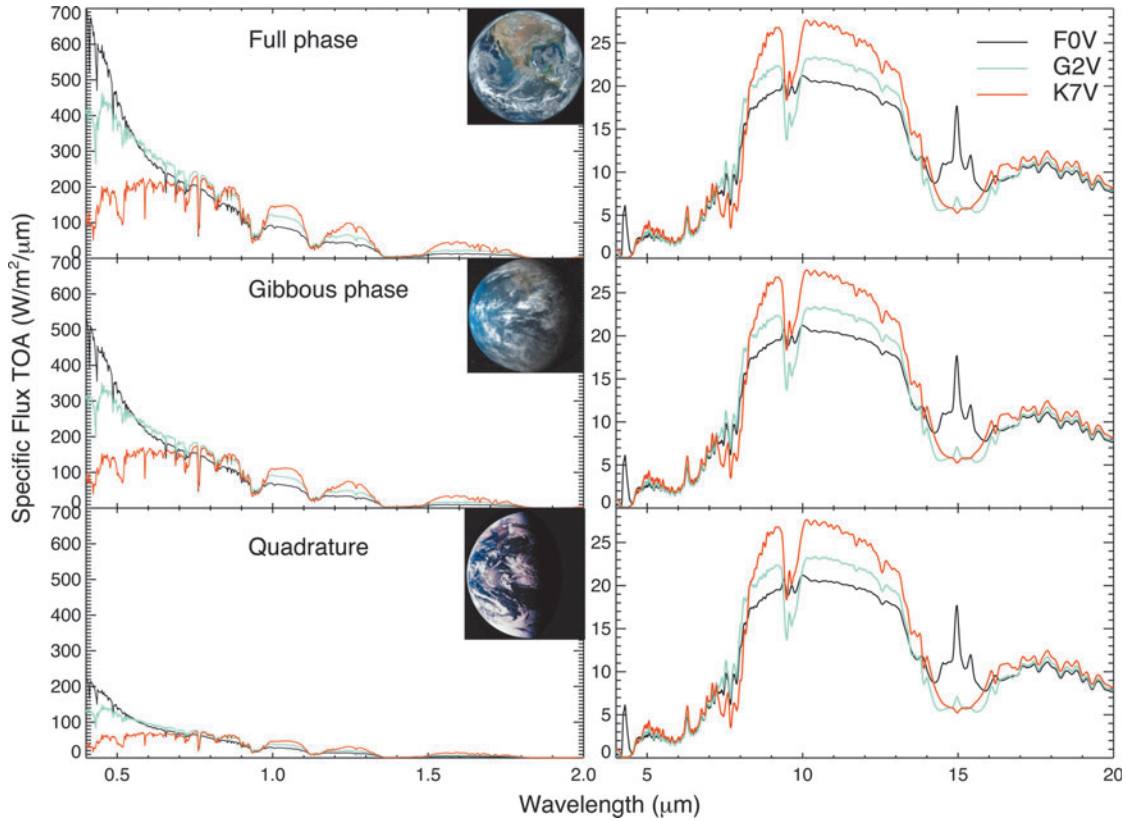
FIG. 15. Absolute specific flux values for 60% cloud coverage Earth-like planets around three different grid stars with $T_{eff} = 7000$, 5750, and 4250 K in the VIS and IR for three phases: full phase, gibbous phase, and quadrature with corresponding phase angles of 0°, 45°, and 90°, respectively. (Color graphics available online at www.liebertonline.com/ast)

absolute specific flux levels at full phase, gibbous phase, and quadrature (phase angles of 0°, 45°, and 90°, respectively) for 60% cloud coverage Earth-like planets orbiting three grid stars with $T_{eff} = 7000$, 5750, and 4250 K to show the effect of orbital position (see also Robinson *et al.*, 2011). For quadrature, representing an average viewing geometry, the contrast ratios presented in Fig. 13 will be a factor of ~ 2 lower in the VIS. Assuming the planet has efficient heat transport from the dayside to nightside, the specific flux levels and contrast ratios in the IR will be unchanged.

6. Conclusions

We calculated the spectra for terrestrial atmosphere models receiving the same incoming flux as Earth when orbiting a grid of host stars with $T_{eff} = 4250$ K to $T_{eff} = 7000$ K in 250 K increments, comprehensively covering the full FGK stellar range. We discussed the detectable features for clear and cloudy atmosphere models and compared the effect of the stars' SED and UV flux on both the atmospheric composition as well as the detectable atmospheric features in Sections 3 and 4.

Increasing UV environments (generally coupled with increasing stellar T_{eff} for main sequence stars) result in increasing concentration of O_3 from photolysis; increasing stratospheric H_2O from O_3 shielding; increasing OH based on increased O_3 and H_2O concentrations; and decreasing CH_4, CH_3Cl, and N_2O from photolysis and reactions with OH. Increasing stellar temperatures and corresponding decreasing planetary surface temperatures result in de-

creasing tropospheric H_2O due to decreased temperatures; decreasing stratospheric H_2O from transport; and decreasing reaction rates of OH with CH_4, N_2O, and CH_3Cl. The overall effect, as the stellar effective temperature of the main sequence grid stars increases, is an increase in O_3 and OH concentration; a decrease in tropospheric H_2O (but an increase stratospheric H_2O); and a decrease in stratospheric CH_4, N_2O, and CH_3Cl.

In the IR, the temperature contrast between the surface and the continuum layer strongly impacts the depth of spectral features. While O_3 increases for hotter main sequence stars, its detectable feature in the IR decreases due to the decrease temperature difference between the continuum and the emitting layer. For hot stars, with $T_{eff} \geq 6750$ K, the O_3 feature appears as emission due to the contrast to the continuum.

Our results provide a grid of atmospheric compositions as well as model spectra from the VIS to the IR for JWST and other future direct detection mission design concepts. The model spectra in this paper are available at www.cfa .harvard.edu/$\sim$srugheimer/FGKSpectra/.

California Institute of Technology, under contract with the National Aeronautics and Space Administration.

Author Disclosure Statement

No competing financial interests exist.

Abbreviations

IUE, International Ultraviolet Explorer; JWST, the James Webb Space Telescope; LW, longwave; SED, spectral energy distribution; SW, shortwave; TOA, top of atmosphere.

References

Batalha, N.M., Rowe, J.F., Bryson, S.T., Barclay, T., Burke, C.J., Caldwell, D.A., Christiansen, J.L., Mullally, F., Thompson, S.E., Brown, T.M., Dupree, A.K., Fabrycky, D.C., Ford, E.B., Fortney, J.J., Gilliland, R.L., Isaacson, H., Latham, D.W., Marcy, G.W., Quinn, S., Ragozzine, D., Shporer, A., Borucki, W.J., Ciardi, D.R., Gautier, T.N., III, Haas, M.R., Jenkins, J.M., Koch, D.G., Lissauer, J.J., Rapin, W., Basri, G.S., Boss, A.P., Buchhave, L.A., Charbonneau, D., Christensen-Dalsgaard, J., Clarke, B.D., Cochran, W.D., Demory, B.-O., Devore, E., Esquerdo, G.A., Everett, M., Fressin, F., Geary, J.C., Girouard, F.R., Gould, A., Hall, J.R., Holman, M.J., Howard, A.W., Howell, S.B., Ibrahim, K.A., Kinemuchi, K., Kjeldsen, H., Klaus, T.C., Li, J., Lucas, P.W., Morris, R.L., Prsa, A., Quintana, E., Sanderfer, D.T., Sasselov, D., Seader, S.E., Smith, J.C., Steffen, J.H., Still, M., Stumpe, M.C., Tarter, J.C., Tenenbaum, P., Torres, G., Twicken, J.D., Uddin, K., Van Cleve, J., Walkowicz, L., and Welsh, W.F. (2012) Planetary candidates observed by Kepler, III: analysis of the first 16 months of data. arXiv:1202.5852v1.

Bates, D.R. and Nicolet, M. (1950) The photochemistry of atmospheric water vapor. J Geophys Res 55:301–310.

Beichman, C.A., Woolf, N.J., and Lindensmith, C.A., editors. (1999) The Terrestrial Planet Finder (TPF): A NASA Origins Program to Search for Habitable Planets, The TPF Science Working Group, National Aeronautics and Space Administration, Washington, DC, and Jet Propulsion Laboratory, California Institute of Technology, Pasadena, CA.

Beichman, C., Lawson, P., Lay, O., Ahmed, A., Unwin, S., and Johnston, K. (2006) Status of the terrestrial planet finder interferometer (TPF-I). Proc SPIE 6268:62680S.

Borucki, W.J., Koch, D.G., Basri, G., Batalha, N., Boss, A., Brown, T.M., Caldwell, D., Christensen-Dalsgaard, J., Cochran, W.D., DeVore, E., Dunham, E.W., Dupree, A.K., Gautier, T.N., III, Geary, J.C., Gilliland, R., Gould, A., Howell, S.B., Jenkins, J.M., Kjeldsen, H., Latham, D.W., Lissauer, J.J., Marcy, G.W., Monet, D.G., Sasselov, D., Tarter, J., Charbonneau, D., Doyle, L., Ford, E.B., Fortney, J., Holman, M.J., Seager, S., Steffen, J.H., Welsh, W.F., Allen, C., Bryson, S.T., Buchhave, L., Chandrasekaran, H., Christiansen, J.L., Ciardi, D., Clarke, B.D., Dotson, J.L., Endl, M., Fischer, D., Fressin, F., Haas, M., Horch, E., Howard, A., Isaacson, H., Kolodziejczak, J., Li, J., MacQueen, P., Meibom, S., Prsa, A., Quintana, E.V., Rowe, J.,

Sherry, W., Tenenbaum, P., Torres, G., Twicken, J.D., Van Cleve, J., Walkowicz, L., and Wu, H. (2011) Characteristics of Kepler planetary candidates based on the first data set. Astrophys J 728, doi:10.1088/0004-637X/728/2/117.

Cash, W. (2006) Detection of Earth-like planets around nearby stars using a petal-shaped occulter. Nature 442:51–53.

Cayrel de Strobel, G., Soubiran, C., Friel, E.D., Ralite, N., and Francois, P. (1997) A catalogue of [Fe/H] determinations: 1996 edition. Astron Astrophys Suppl Ser 124:299–305.

Cayrel de Strobel, G., Soubiran, C., and Ralite, N. (2001) Catalogue of [Fe/H] determinations for FGK stars: 2001 edition. Astron Astrophys Suppl Ser 373:159–163.

Chapman, S. (1930) A theory of upper atmospheric ozone. Memoirs of the Royal Meteorological Society 3:103–125.

Crutzen, P.J. (1970) Influence of nitrogen oxides on atmospheric ozone content. Quarterly Journal of the Royal Meteorological Society 96:320–325.

Deming, D., Seager, S., Winn, J., Miller-Ricci, E., Clampin, M., Lindler, D., Greene, T., Charbonneau, D., Laughlin, G., Ricker, G., Latham, D., and Ennico, K. (2009) Discovery and characterization of transiting super Earths using an all-sky transit survey and follow-up by the James Webb Space Telescope. Publ Astron Soc Pac 121:952–967.

Des Marais, D.J., Harwit, M., Jucks, K., Kasting, J.F., Lin, D., Lunine, J., Schneider, J., Seager, S., Traub, W., and Woolf, N. (2002) Remote sensing of planetary properties and biosignatures on extrasolar terrestrial planets. Astrobiology 2:153–181.

Di Folco, E. Thévenin, F., Kervella, P., Domiciano de Souza, A., Coudé du Foresto, V., Ségransan, D., and Morel, P. (2004) VLTI near-IR interferometric observations of Vega-like stars. Radius and age of α PsA, β Leo, β Pic, ε Eri and τ Cet. Astron Astrophys 426:601–617.

Flower, P.J. (1996) Transformations from theoretical Hertzsprung-Russell diagrams to color-magnitude diagrams: effective temperatures, B-V colors, and bolometric corrections. Astrophys J 469:355.

Forster, P., Ramaswamy, V., Artaxo, P., Berntsen, T., Betts, R., Fahey, D.W., Haywood, J., Lean, J., Lowe, D.C., Myhre, G., Nganga, J., Prinn, R., Raga, G., Schulz, M., and Van Dorland, R. (2007) Changes in atmospheric constituents and in radiative forcing. In Climate Change 2007: The Physical Science Basis. Contribution of Working Group I to the Fourth Assessment Report of the Intergovernmental Panel on Climate Change, edited by S. Solomon, D. Qin, M. Manning, Z. Chen, M. Marquis, K.B. Averyt, M. Tignor, and H.L. Miller, Cambridge University Press, Cambridge, UK, pp 129–215.

Gardner, J.P., Mather, J.C., Clampin, M., Doyon, R., Greenhouse, M.A., Hammel, H.B., Hutchings, J.B., Jakobsen, P., Lilly, S.J., Long, K.S., Lunine, J.I., McCaughrean, M.J., Mountain, M., Nella, J., Rieke, G.H., Rieke, M.J., Rix, H., Smith, E.P., Sonneborn, G., Stiavelli, M., Stockman, H.S., Windhorst, R.A., and Wright, G.S. (2006) The James Webb Space Telescope. Space Sci Rev 123:485–606.

Gray, D. (1992) Global stellar parameters: parameters for main-sequence stars. In The Observation and Analysis of Stellar Photospheres, Cambridge University Press, Cambridge, UK, p 431.

Grenfell, J.L., Stracke, B., von Paris, P., Patzer, B., Titz, R., Segura, A., and Rauer, H. (2007) The response of atmospheric chemistry on Earthlike planets around F, G and K stars to small variations in orbital distance. Planet Space Sci 55:661–671.

Haqq-Misra, J., Domagal-Goldman, S., Kasting, P., and Kasting, J. (2008) A revised, hazy methane greenhouse for the early Earth. Astrobiology 8:1127–1137.

Hartmann, L. and Anderson, C.M. (1977) Abundances in late-type dwarfs. *Astrophys J* 215:188–193.

Houghton, J.T., Meira Filho, L.G., Bruce, J., Lee, H., Callander, B.A., Haites, E., Harris, N., and Maskell, K., editors. (1994) *Climate Change, 1994: Radiative Forcing of Climate Change and an Evaluation of the IPCC IS92 Emission Scenarios*, Cambridge University Press, Cambridge, UK.

Kaltenegger, L. (2010) Characterizing habitable exo-moons. *Astrophys J* 711:L1–L6.

Kaltenegger, L. and Sasselov, D. (2010) Detecting planetary geochemical cycles on exoplanets: atmospheric signatures and the case of SO_2. *Astrophys J* 708:1162–1167.

Kaltenegger, L. and Sasselov, D. (2011) Exploring the habitable zone for Kepler planetary candidates. *Astrophys J* 736:L25.

Kaltenegger, L. and Traub, W.A. (2009) Transits of Earth-like planets. *Astrophys J* 698:519–527.

Kaltenegger, L., Traub, W.A., and Jucks, K.W. (2007) Spectral evolution of an Earthlike planet. *Astrophys J* 658, doi:10.1086/510996.

Kaltenegger, L., Selsis, F., Fridlund, M., Lammer, H., Beichman, C., Danchi, W., Eiroa, C., Henning, T., Herbst, T., Léger, A., Liseau, R., Lunine, J., Paresce, F., Penny, A., Quirrenbach, A., Röttgering, H., Schneider, J., Stam, D., Tinetti, G., and White, G.J. (2010a) Deciphering spectral fingerprints of habitable exoplanets. *Astrobiology* 10:89–102.

Kaltenegger, L., Henning, W.G., and Sasselov, D. (2010b) Detecting volcanism on extrasolar planets. *Astron J* 140:1370–1380.

Kasting, J.F. and Ackerman, T.P. (1986) Climatic consequences of very high CO_2 levels in the Earth's early atmosphere. *Science* 234:1383–1385.

Kasting, J.F., Pollack, J.B., and Crisp, D. (1984) Effects of high CO_2 levels on surface temperature and atmospheric oxidation state on the early Earth. *J Atmos Chem* 1:403–428.

Kasting, J.F., Holland, H.D., and Pinto, J.P. (1985) Oxidant abundances in rainwater and the evolution of atmospheric oxygen. *J Geophys Res* 90:10497–10510.

Kitzmann, D., Patzer, A.B.C., von Paris, P., Godolt, M., and Rauer, H. (2011a) Clouds in the atmospheres of extrasolar planets: II. Thermal emission spectra of Earth-like planets influenced by low and high-level clouds. *Astron Astrophys* 531:A62.

Kitzmann, D., Patzer, A.B.C., von Paris, P., Godolt, M., and Rauer, H. (2011b) Clouds in the atmospheres of extrasolar planets: III. Impact of low and high-level clouds on the reflection spectra of Earth-like planets. *Astron Astrophys* 534:A63.

Kurucz, R.L. (1979) Model atmospheres for G, F, A, B, and O stars. *Astrophys J Suppl Ser* 40:1–340.

Livengood, T.A., Deming, L.D., A'Hearn, M.F., Charbonneau, D., Hewagama, T., Lisse, C.M., McFadden, L.A., Meadows, V.S., Robinson, T.D., Seager, S., and Wellnitz, D.D. (2011) Properties of an Earth-like planet orbiting a Sun-like star: Earth observed by the EPOXI mission. *Astrobiology* 11:907–930.

Lovelock, J.E. (1975) Thermodynamics and the recognition of alien biospheres. *Proc R Soc Lond B Biol Sci* 189:167–180.

Massa, D. and Fitzpatrick, E.L. (2000) A recalibration of IUE NEWSIPS low-dispersion data. *Astrophys J Suppl Ser* 126:517–535.

Massa, D., Van Steenberg, M.E., Oliversen, N., and Lawton, P. (1998) Science verification of the IUE Final Archive data products. In *Special Publication 413: UV Astrophysics Beyond the IUE Final Archive*, edited by W. Wamsteker and R. Gonzalez Riestra, ESA Publications Division, Noordwijk, the Netherlands, pp 723–726.

Meadows, V.S. (2006) Modeling the diversity of extrasolar terrestrial planets. Direct imaging of exoplanets: science and techniques. In *Proceedings of the IAU Colloquium,* No. 200, Cambridge University Press, Cambridge, UK, pp 25–34.

Molina, M.J. and Rowland, F.S. (1974) Stratospheric sink for chlorofluoromethanes: chlorine atom catalyzed destruction of ozone. *Nature* 249:810–814.

Pallé, E., Ford, E.B., Seager, S., Montañés-Rodríguez, P., and Vazquez, M. (2008) Identifying the rotation rate and the presence of dynamic weather on extrasolar Earth-like planets from photometric observations. *Astrophys J* 676:1319–1329.

Pavlov, A.A. and Kasting, J.F. (2002) Mass-independent fractionation of sulfur isotopes in Archean sediments: strong evidence for an anoxic Archean atmosphere. *Astrobiology* 2:27–41.

Pavlov, A., Kasting, J., Brown, L., Rages, K., and Freedman, R. (2000) Greenhouse warming by CH_4 in the atmosphere of early Earth. *J Geophys Res* 105:11981–11990.

Pavlov, A.A., Hurtgen, M.T., Kasting, J.F., and Arthur, M.A. (2003) Methane-rice Proterozoic atmosphere? *Geology* 31:87–90.

Robinson, T.D., Meadows, V.S., Crisp, D., Deming, L.D., A'Hearn, M.F., Charbonneau, D., Livengood, T.A., Seager, S., Barry, R.K., Hearty, T., Hewagama, T., Lisse, C.M., McFadden, L.A., and Wellnitz, D.D. (2011) Earth as an exoplanet: Earth model validation using EPOXI Earth observations. *Astrobiology* 11:393–408.

Sagan, C., Thompson, W.R., Carlson, R., Gurnett, D., and Hord, C. (1993) A search for life on Earth from the Galileo spacecraft. *Nature* 365:715–721.

Schindler, T.L. and Kasting, J.F. (2000) Synthetic spectra of simulated terrestrial atmospheres containing possible biomarker gases. *Icarus* 145:262–271.

Seager, S., Turner, E.L., Schafer, J., and Ford, E.B. (2005) Vegetation's red edge: a possible biomarker of extraterrestrial plants. *Astrobiology* 5:372–390.

Segura, A., Krelove, K., Kasting, J.F., Sommerlatt, D., Meadows, V., Crisp, D., Cohen, M., and Mlawer, E. (2003) Ozone concentrations and ultraviolet fluxes on Earth-like planets around other stars. *Astrobiology* 3:689–708.

Segura, A., Kasting, J.F., Meadows, V., Cohen, M., Scalo, J., Crisp, D., Butler, R.A.H., and Tinetti, G. (2005) Biosignatures from Earth-like planets around M dwarfs. *Astrobiology* 5:706–725.

Segura, A., Meadows, V.S., Kasting, J.F., Crisp, D., and Cohen, M. (2007) Abiotic formation of O_2 and O_3 in high-CO_2 terrestrial atmospheres. *Astron Astrophys* 472:665–679.

Segura, A., Walkowicz, L.M., Victoria Meadows, V., Kasting, J., and Hawley, S. (2010) The effect of a strong stellar flare on the atmospheric chemistry of an Earth-like planet orbiting an M dwarf. *Astrobiology* 10:751–771.

Selsis, F. (2000) Review: physics of planets I: Darwin and the atmospheres of terrestrial planets. In *Darwin and Astronomy—The Infrared Space Interferometer*, ESA SP 451, ESA Publications Division, Noordwijk, the Netherlands, pp 133–142.

Sneep, M. and Ubachs, W. (2004) Direct measurement of the Rayleigh scattering cross section in various gases. *J Quant Spectrosc Radiat Transf* 92:293–310.

Toon, O.B., McKay, C.P., Ackerman, T.P., and Santhanam, K. (1989) Rapid calculation of radiative heating rates and photodissociation rates in inhomogeneous multiple scattering atmospheres. *J Geophys Res* 94:16287–16301.

Traub, W.A. and Stier, M.T. (1976) Theoretical atmospheric transmission in the mid- and far-infrared at four altitudes. *Appl Opt* 15:364–377.

Traub, W.A., Levine, M., Shaklan, S., Kasting, J., Angel, J.R., Brown, M.E., Brown, R.A., Burrows, C., Clampin, M., Dressler, A., Ferguson, H.C., Hammel, H.B., Heap, S.R., Horner, S.D., Illingworth, G.D., Kasdin, N.J., Kuchner, M.J., Lin, D., Marley, M.S., Meadows, V., Noecker, C., Oppenheimer, B.R., Seager, S., Shao, M., Stapelfeldt, K.R., and Trauger, J.T. (2006) TPF-C: status and recent progress. *Proc SPIE* 6268, doi:10.1117/12.673608.

Udry, S., Bonfils, X., Delfosse, X., Forveille, T., Mayor, M., Perrier, C., Bouchy, F., Lovis, C., Pepe, F., Queloz, D., and Bertaux, J.-L. (2007) The HARPS search for southern extra-solar planets. XI. Super-Earths (5 and 8 $M_\oplus$) in a 3-planet system. *Astron Astrophys* 469:L43–L47.

Valenti, J.A. and Fischer, D.A., (2005) Spectroscopic Properties of Cool Stars (SPOCS). I. 1040 F, G, and K Dwarfs from Keck, Lick, and AAT Planet Search Programs. *Astrophys J Suppl Ser* 159:141–166.

Address correspondence to:
Sarah Rugheimer
Center for Astrophysics
60 Garden St. MS 10
Cambridge, MA 02138
USA

E-mail: srugheimer@cfa.harvard.edu